

A Petrov-Galerkin Spectral Element Method for Fractional Elliptic Problems

Ehsan Kharazmi^{a,b}, Mohsen Zayernouri^{a,b,*} and George Em Karniadakis^c

^a Department of Computational Mathematics, Science, and Engineering &

^b Department of Mechanical Engineering

Michigan State University, 428 S Shaw Ln, East Lansing, MI 48824

^c Division of Applied Mathematics, Brown University, 182 George, Providence, RI 02912, USA

Abstract

We develop a new C^0 -continuous Petrov-Galerkin spectral element method for one-dimensional fractional elliptic problems of the form ${}_0\mathcal{D}_x^\alpha u(x) - \lambda u(x) = f(x)$, $\alpha \in (1, 2]$, subject to homogeneous boundary conditions. We employ the standard (modal) spectral element bases and the Jacobi poly-fractionomials as the test functions [1]. We formulate a new procedure for assembling the global linear system from elemental (local) mass and stiffness matrices. The Petrov-Galerkin formulation requires performing elemental (local) construction of mass and stiffness matrices in the standard domain only once. Moreover, we efficiently obtain the non-local (history) stiffness matrices, in which the non-locality is presented analytically for uniform grids. We also investigate two distinct choices of basis/test functions: i) local basis/test functions, and ii) local basis with global test functions. We show that the former choice leads to a better-conditioned system and accuracy. We consider smooth and singular solutions, where the singularity can occur at boundary points as well as in the interior domain. We also construct two non-uniform grids over the whole computational domain in order to capture singular solutions. Finally, we perform a systematic numerical study of non-local effects via full and partial history fading in order to further enhance the efficiency of the scheme.

Keywords: C^0 -continuous element, modal basis/test functions, non-local assembling/scattering, boundary/interior singularities, history fading analysis, spectral convergence

1. Introduction

Fractional order models open up new possibilities for robust mathematical modeling of complex multi-scale problems and anomalous transport phenomena including: non-Markovian (Lévy flights) processes in turbulent flows [2, 3], non-Newtonian fluids and rheology [4], non-Brownian transport phenomena in porous and disordered materials [5, 6], non-Gaussian processes in multi-scale complex fluids and multi-phase applications [7], visco-elastic bio-tissues, and visco-elasto-plastic materials [6, 8, 9].

A number of local numerical methods, prominently finite difference methods (FDMs), have been developed for solving fractional partial differential equations (FPDEs) [10, 11, 12, 13, 14, 15, 16, 17, 18, 19, 20, 21, 22, 23, 24, 25]. Fix and Roop [26] developed the first theoretical framework for the least-square finite element method (FEM) approximation of a fractional-order differential equation, where optimal error estimates are proven for piecewise linear elements. However, Roop [27] later showed that the main hurdle to overcome in the FEM is the non-local nature of the fractional operator, which leads to large dense matrices; he showed that even the construction of such matrices presents difficulties. Ervin and Roop [28] presented a theoretical framework for the variational solution of the steady state fractional advection dispersion equation based on FEM and proved the existence and uniqueness of the results. Jin et al. [29] proved the existence and uniqueness of a weak solution to the space-fractional parabolic equation using FEM; they showed an enhanced regularity of the solution and derived the error estimate for both semidiscrete and fully discrete solution. Well-posedness, regularity of the weak solution, stability of the discrete variational formulation and error estimate of the FEM approximation were investigated for fractional elliptic problems in [30]. Wang and Yang [31] generalized the analysis to the case of fractional elliptic problems with variable coefficient, analyzed the regularity of the solution in Hölder spaces, and established the well-posedness of a Petrov-Galerkin formulation. Wang et al. [32] developed an indirect FEM for the Dirichlet boundary-value problems of Caputo FPDEs showing the reduction in the computational work for numerical solution and memory requirements.

There has been recently more attention and effort put on developing global and high-order approximations, which are capable of efficiently capturing the inherent non-local effects. A Chebyshev spectral element method (SEM) for fractional-order transport was adopted by Hanert [33] and later on, the idea of least-square

*Corresponding Author: zayern@msu.edu

FEM was extended to SEM by Carella [34]. More recently, Deng and Hesthaven [35] and Xu and Hesthaven [36] developed local DG methods for solving space-fractional diffusion and convection-diffusion problems.

Two new spectral theories on fractional and tempered fractional Sturm-Liouville problems (TFSLPs) have been developed by Zayernouri et al. in [1, 37]. This approach first fractionalizes and then tempers the well-known theory of Sturm-Liouville eigen-problems. The explicit eigenfunctions of TFSLPs are analytically obtained in terms of *tempered Jacobi poly-fractonomials*. These poly-fractonomials have been successfully employed in developing a series of high-order and efficient Petrov-Galerkin spectral and discontinuous spectral element methods [38, 39, 40]. In [41], Zayernouri and Karniadakis developed a spectral and spectral element method for FODEs with an exponential accuracy. They also developed a highly accurate discontinuous SEM for time- and space- fractional advection equation in [38]. Dehghan et al. [42] considered Legendre SEM in space and FDM in time for solving time-fractional sub-diffusion equation. Su [43] provided a parallel spectral element method for the fractional Lorenz system and a comparison of the method with FEM and FDM.

The SEM discretization has the benefit of domain decomposition into non-overlapping elements, which potentially provide a geometrical flexibility, especially for adaptivity as well as complex domains. Moreover, high-order approximations within each element yield a fast rate of convergence even in the cases of non-smooth and/or rapid transients in the solution. Therefore, a tractable computational cost of the method can be achieved by a successful combination of *h-refinement*, where the solution is rough, and *p-refinement*, where the solution is smooth.

In the present work, we consider the one-dimensional space-fractional Helmholtz equation of order $\alpha \in (1, 2]$ subject to homogeneous boundary conditions. We formulate a weak form, in which the fractional portion $\mu \in (0, 1]$ is transferred onto some proper fractional order test functions via integration-by-parts. This setting enables us to employ the standard polynomial modal basis functions, used in SEM [44]. Subsequently, we develop a new C^0 -continuous Petrov-Galerkin SEM, following the recent spectral theory of fractional Sturm-Liouville problem, where the test functions are of Jacobi poly-fractonomials of second kind [1]. We investigate two distinct choices of basis/test functions: i) *local* basis/test functions, and ii) *local* basis with *global* test functions, which enables the construction of elemental mass/stiffness matrices in the standard domain $[-1, 1]$. We explicitly compute the elemental stiffness matrices using the orthogonality of Jacobi polynomials. Moreover, we efficiently obtain the non-local (history) stiffness matrices, in which the

non-locality is presented *analytically*. On one hand, we formulate a new *non-local assembling procedure* in order to construct the global linear system from the local (elemental) mass/stiffness matrices and history matrices. On the other hand, we formulate a procedure for *non-local scattering* to obtain the elemental expansion coefficients from the global degrees of freedom. We demonstrate the efficiency of the Petrov-Galerkin methods and show that the choice of local bases/test functions leads to a better accuracy and conditioning. Moreover, for uniform grids, we compute the history matrices off-line. The stored history matrices can be retrieved later in the construction of the global linear system. We show the great improvement in the computational cost by performing the retrieval procedure compared to on-line computation. We also introduce a non-uniform *kernel-based* grid generation in addition to *geometrically progressive* grid generation approaches. Furthermore, we investigate the performance of the developed schemes by considering two cases of smooth and singular solutions, where the singularity can occur at boundary points or the interior domain. Finally, we study the effect of history fading via a systematic analysis, where we consider the history up to some specific element and let the rest fade. This results in less computational cost, while we show that the accuracy is still preserved. The main contributions of this work are listed in the following:

- Development of a new fast and accurate C^0 -continuous Petrov-Galerkin spectral element method, employing local basis/test functions, where the test functions are Jacobi poly-fractonomials.
- Reducing the number of history calculation from $\frac{N_{el}(N_{el}-1)}{2}$ to $(N_{el} - 1)$ for a uniformly partitioned domain.
- Analytical expression of non-local effects in uniform grids leading to fast computation of the history matrices.
- A new procedure for the assembly of the global linear system.
- Performing off-line computation of history matrices and on-line retrieval of the stored matrices.
- Boundary and interior singularity capturing using adaptive *hp*-refinement.
- Non-uniform kernel-based grid generation for resolving steep gradients and singularities.

The organization of the paper is as follows: section 2 provides preliminary definitions including problem definition, derivation of the weak form and expressions for the local basis and local/global test functions. In section 3, we present a Petrov-Galerkin method employing the local basis/test functions in addition to formulating the non-local assembling and non-local scattering procedures, followed by a discussion on how to compute *off-line* the history matrices. We also present the two non-uniform grid generation approaches. In section 4, we present a Petrov-Galerkin method employing the local basis with global test functions, compared with the former scheme. In section 5, we demonstrate the computational efficiency of the methods by considering several numerical examples of smooth and singular solutions. Finally, we perform the off-line computation and retrieval procedure of history matrices and a systematic history fading analysis. We end the paper with a summary.

2. Definitions

Let $\xi \in [-1, 1]$. Then, the left-sided and right-sided Riemann-Liouville integrals of order σ , $n - 1 < \sigma \leq n$, $n \in \mathbb{N}$, are defined (see e.g., [45, 46]) respectively as

$$({}_{-1}^{RL}I_{\xi}^{\sigma})u(\xi) = \frac{1}{\Gamma(\sigma)} \int_{-1}^{\xi} \frac{u(s)ds}{(\xi - s)^{n-\sigma}}, \quad \xi > -1, \quad (1)$$

and

$$({}_{\xi}^{RL}I_1^{\sigma})u(\xi) = \frac{1}{\Gamma(\sigma)} \int_{\xi}^1 \frac{u(s)ds}{(s - \xi)^{n-\sigma}}, \quad \xi < 1. \quad (2)$$

The corresponding left-sided and right-sided fractional derivatives of order σ are then defined as

$$({}_{-1}^{RL}\mathcal{D}_{\xi}^{\sigma})u(\xi) = \frac{d^n}{d\xi^n}({}_{-1}^{RL}I_{\xi}^{n-\sigma}u)(\xi) = \frac{1}{\Gamma(n-\sigma)} \frac{d^n}{d\xi^n} \int_{-1}^{\xi} \frac{u(s)ds}{(\xi - s)^{\sigma+1-n}}, \quad \xi > -1, \quad (3)$$

and

$$({}_{\xi}^{RL}\mathcal{D}_1^{\sigma})u(\xi) = \frac{(-d)^n}{d\xi^n}({}_{\xi}^{RL}I_1^{n-\sigma}u)(\xi) = \frac{1}{\Gamma(n-\sigma)} \frac{(-d)^n}{d\xi^n} \int_{\xi}^1 \frac{u(s)ds}{(s - \xi)^{\sigma+1-n}}, \quad \xi < 1, \quad (4)$$

respectively.

By performing an affine mapping from the standard domain $[-1, 1]$ to the interval $x \in [x_{\varepsilon-1}, x_{\varepsilon}]$, we obtain

$${}_{x_{\varepsilon-1}}^{RL}\mathcal{D}_{x_{\varepsilon}}^{\mu}u = \left(\frac{2}{x_{\varepsilon} - x_{\varepsilon-1}}\right)^{\mu}({}_{-1}^{RL}\mathcal{D}_{\xi}^{\mu}u)(\xi). \quad (5)$$

Hence, we can perform the operations in the standard domain only once for any given σ and efficiently utilize them on any arbitrary interval without resorting to repeating the calculations.

We define the *Jacobi poly-fractonomials* (of second kind), used as the test functions in developing the proposed numerical schemes following the recent theory of fractional Sturm-Liouville eigen-problems (FSLP) in [1]. The corresponding regular poly-fractonomials are given in the standard domain $[-1, 1]$ by

$${}^{(2)}\mathcal{P}_k^\mu(\xi) = (1 - \xi)^\mu P_{k-1}^{\mu, -\mu}(\xi), \quad \xi \in [-1, 1], \quad (6)$$

where $P_{k-1}^{\mu, -\mu}$ is the Jacobi Polynomial.

2.1. Problem Definition

We study the following fractional Helmholtz equation of order $\alpha = 1 + \mu$, $\mu \in (0, 1]$:

$${}^{RL}_0\mathcal{D}_x^\alpha u(x) - \lambda u(x) = f(x), \quad \forall x \in \Omega \quad (7)$$

$$u(0) = u(L) = 0, \quad \forall x \in \partial\Omega, \quad (8)$$

where $\Omega = [0, L]$. By multiplying both sides of (7) by some proper test function $v(x)$, then taking the fractional integration-by-parts, we obtain the following bilinear form:

$$a(u, v) = l(v), \quad (9)$$

in which

$$a(u, v) = \left(\frac{du}{dx}, {}^{RL}_x\mathcal{D}_L^\mu v \right)_\Omega - \lambda (u, v)_\Omega, \quad (10)$$

$$l(v) = (f, v)_\Omega, \quad (11)$$

where $(\cdot, \cdot)_\Omega$ denotes the well-known inner-product.

2.2. Local Basis Functions

We partition the computational domain into N_{el} non-overlapping elements $\Omega_e = [x_{e-1}, x_e]$ such that $\Omega = \cup_{e=1}^{N_{el}} \Omega_e$, see Fig. 1. Therefore, the bilinear form (10) can be written as

$$a(u, v) \approx a(u^\delta, v^\delta) = \sum_{e=1}^{N_{el}} \left(\frac{du_N^{(e)}}{dx}, {}^{RL}_x\mathcal{D}_L^\mu v^\delta \right)_{\Omega_e} - \lambda \sum_{e=1}^{N_{el}} \left(u_N^{(e)}, v^\delta \right)_{\Omega_e}, \quad (12)$$

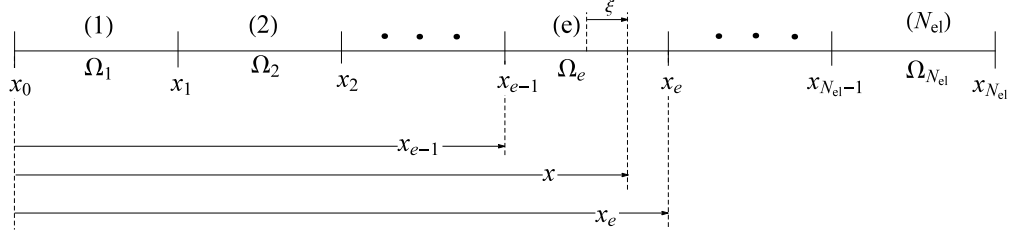


Figure 1: Domain partitioning

where we approximate the solution in each element as

$$u_N^{(e)}(x) = \sum_{p=0}^P \hat{u}_p^{(e)} \Psi_p(x), \quad x \in \Omega_e, \quad (13)$$

and thus, the approximated solution over the whole domain is

$$u \approx u^\delta(x) = \sum_{e=1}^{N_{el}} \sum_{p=0}^P \hat{u}_p^{(e)} \Psi_p(x). \quad (14)$$

We choose the $P+1$ modal basis functions $\Psi_p(x)$, defined in the standard element in terms of $\zeta \in [-1, 1]$ as

$$\Psi_p(\zeta) = \begin{cases} \frac{1-\zeta}{2}, & p = 0, \\ \left(\frac{1-\zeta}{2}\right)\left(\frac{1+\zeta}{2}\right) P_{p-1}^{1,1}(\zeta), & p = 1, 2, \dots, P-1, \\ \frac{1+\zeta}{2}, & p = P, \end{cases} \quad (15)$$

which are also used in standard spectral element methods for integer-order PDEs (see e.g., [44]).

2.3. Test Functions: Local vs. Global

We choose two types of test functions v^δ : i) *local* test functions, and ii) *global* test functions, defined for $\varepsilon = 1, 2, \dots, N_{el}$ as follows:

$$v_k^{local}(x) = v_k^\varepsilon(x) = \begin{cases} {}^{(2)}\mathcal{P}_{k+1}^\mu(x^\varepsilon), & \forall x \in \Omega_\varepsilon, \\ 0, & \text{otherwise,} \end{cases}, \quad k = 0, 1, \dots, P, \quad (16)$$

in which ${}^{(2)}\mathcal{P}_{k+1}^\mu(x^\varepsilon)$ represents the Jacobi *poly-fractonomial* of second kind, defined in the corresponding intervals $\Omega_\varepsilon = [x_{\varepsilon-1}, x_\varepsilon]$, using (6); and

$$v_k^{global}(x) = v_k^\varepsilon(x) = \begin{cases} {}^{(2)}\mathcal{P}_{k+1}^\mu(x^{1\sim\varepsilon}), & \forall x \in [0, x_\varepsilon], \\ 0, & \text{otherwise} \end{cases}, \quad k = 0, 1, \dots, P, \quad (17)$$

where ${}^{(2)}\mathcal{P}_{k+1}^\mu(x^{1\sim\varepsilon})$ represents the Jacobi *poly-fractonomial* of second kind, defined in the corresponding intervals $[0, x_\varepsilon]$, using (6). It should be noted that for each element ε , the corresponding local test function has nonzero value only in the element and vanishes elsewhere, unlike the corresponding global test function, which vanishes only where $x > x_\varepsilon$.

3. Petrov-Galerkin Method with Local Test Functions

By substituting (13) and (16) into (12), we obtain:

$$\begin{aligned} & \sum_{e=1}^{N_{el}} \left(\sum_{p=0}^P \hat{u}_p^{(e)} \frac{d\Psi_p(x)}{dx}, {}^{RL}\mathcal{D}_L^\mu v_k^\varepsilon(x) \right)_{\Omega_e} - \lambda \sum_{e=1}^{N_{el}} \left(\sum_{p=0}^P \hat{u}_p^{(e)} \Psi_p(x), v_k^\varepsilon(x) \right)_{\Omega_e} \\ & = \left(f, v_k^\varepsilon(x) \right)_{\Omega}, \quad \varepsilon = 1, 2, \dots, N_{el}, \quad k = 0, 1, \dots, P. \end{aligned} \quad (18)$$

Since the local test function vanishes $\forall x \in \Omega_e \neq \Omega_\varepsilon$, we have

$$\begin{aligned} \lambda \sum_{e=1}^{N_{el}} \left(\sum_{p=0}^P \hat{u}_p^{(e)} \Psi_p(x), v_k^\varepsilon(x) \right)_{\Omega_e} & = \lambda \left(\sum_{p=0}^P \hat{u}_p^{(\varepsilon)} \Psi_p(x), v_k^\varepsilon(x) \right)_{\Omega_\varepsilon}, \\ \left(f, v_k^\varepsilon(x) \right)_{\Omega} & = \left(f, v_k^\varepsilon(x) \right)_{\Omega_\varepsilon}. \end{aligned}$$

Moreover, for every ε , the right-sided fractional derivative,

$${}^{RL}\mathcal{D}_L^\mu v_k^\varepsilon(x) = \frac{-1}{\Gamma(1-\mu)} \frac{d}{dx} \int_x^L \frac{v_k^\varepsilon(s)}{(s-x)^\mu} ds, \quad x \in \Omega_e,$$

is taken from $x \in \Omega_e$ to $x = L$, where $e = 1, 2, \dots, N_{el}$ through the summation over the elements and s varies from $x \in \Omega_e$ to L . The local test function vanishes $\forall x \in \Omega_e \neq \Omega_\varepsilon$, thus if $e > \varepsilon$ ($x > x_\varepsilon$, see Fig. 2 top), then

$${}^{RL}\mathcal{D}_L^\mu v_k^\varepsilon(x) = \frac{-1}{\Gamma(1-\mu)} \frac{d}{dx} \int_x^L \frac{0}{(s-x)^\mu} ds = 0, \quad (19)$$

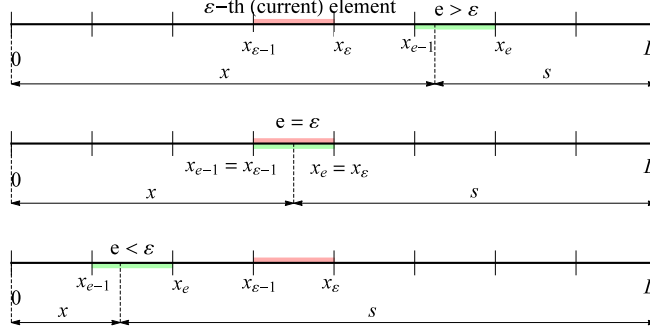


Figure 2: Location of the (dummy) element number, e , with respect to the current element, ε . If $e > \varepsilon$, (top), then ${}^{RL}\mathcal{D}_x^\mu v_k^\varepsilon(x) = 0$. If $e = \varepsilon$, (middle), then ${}^{RL}\mathcal{D}_x^\mu v_k^\varepsilon(x) = {}^{RL}\mathcal{D}_{x_\varepsilon}^\mu \left[({}^{(2)}\mathcal{P}_{k+1}^\mu(x)) \right]$. If $e < \varepsilon$, (bottom), then ${}^{RL}\mathcal{D}_x^\mu v_k^\varepsilon(x) = H_k^{(\varepsilon)}(x)$.

and if $e < \varepsilon$ ($x < x_{\varepsilon-1}$, see Fig. 2 bottom), then

$${}^{RL}\mathcal{D}_x^\mu v_k^\varepsilon(x) = \frac{-1}{\Gamma(1-\mu)} \frac{d}{dx} \int_{x_{\varepsilon-1}}^{x_\varepsilon} \frac{({}^{(2)}\mathcal{P}_{k+1}^\mu(s))}{(s-x)^\mu} ds \equiv H_k^{(\varepsilon)}(x), \quad (20)$$

and if $e = \varepsilon$, ($x_{\varepsilon-1} < x < x_\varepsilon$, see Fig. 2 middle), then

$${}^{RL}\mathcal{D}_x^\mu v_k^\varepsilon(x) = \frac{-1}{\Gamma(1-\mu)} \frac{d}{dx} \int_x^{x_\varepsilon} \frac{({}^{(2)}\mathcal{P}_{k+1}^\mu(s))}{(s-x)^\mu} ds = {}^{RL}\mathcal{D}_{x_\varepsilon}^\mu \left[({}^{(2)}\mathcal{P}_{k+1}^\mu(x)) \right]. \quad (21)$$

Hence, for $\varepsilon = 1, 2, \dots, N_{el}$ and $k = 0, 1, \dots, P$,

$${}^{RL}\mathcal{D}_x^\mu v_k^\varepsilon(x) = \begin{cases} 0, & \forall x \in \Omega_e, e > \varepsilon, \\ {}^{RL}\mathcal{D}_{x_\varepsilon}^\mu \left[({}^{(2)}\mathcal{P}_{k+1}^\mu(x)) \right], & \forall x \in \Omega_e, e = \varepsilon, \\ H_k^{(\varepsilon)}(x), & \forall x \in \Omega_e, e < \varepsilon. \end{cases} \quad (22)$$

Therefore, the bilinear form (18) can be written as

$$\begin{aligned} & \sum_{e=1}^{\varepsilon-1} \sum_{p=0}^P \hat{u}_p^{(e)} \left(\frac{d\Psi_p(x)}{dx}, H_k^{(\varepsilon)}(x) \right)_{\Omega_e} + \sum_{p=0}^P \hat{u}_p^{(\varepsilon)} \left(\frac{d\Psi_p(x)}{dx}, {}^{RL}\mathcal{D}_{x_\varepsilon}^\mu \left[({}^{(2)}\mathcal{P}_{k+1}^\mu(x)) \right] \right)_{\Omega_\varepsilon} \\ & - \lambda \sum_{p=0}^P \hat{u}_p^{(\varepsilon)} \left(\Psi_p(x), ({}^{(2)}\mathcal{P}_{k+1}^\mu(x)) \right)_{\Omega_\varepsilon} = \left(f, ({}^{(2)}\mathcal{P}_{k+1}^\mu(x)) \right)_{\Omega_\varepsilon}, \end{aligned} \quad (23)$$

and the weak form is obtained as

$$\sum_{e=1}^{\varepsilon-1} \sum_{p=0}^P \hat{u}_p^{(e)} \hat{\mathbf{S}}_{kp}^{(e,\varepsilon)} + \sum_{p=0}^P \hat{u}_p^{(\varepsilon)} \left[\mathbf{S}_{kp}^{(\varepsilon)} - \lambda \mathbf{M}_{kp}^{(\varepsilon)} \right] = \mathbf{f}_k^{(\varepsilon)}, \quad \begin{cases} \varepsilon = 1, 2, \dots, N_{el}, \\ k = 0, 1, \dots, P, \end{cases} \quad (24)$$

in which

$$\begin{aligned} \hat{\mathbf{S}}_{kp}^{(e,\varepsilon)} &= \left(\frac{d\Psi_p}{dx}, H_k^{(\varepsilon)}(x) \right)_{\Omega_e}, \quad e = 1, 2, \dots, \varepsilon - 1, \\ \mathbf{S}_{kp}^{(\varepsilon)} &= \left(\frac{d\Psi_p}{dx}, {}^{RL}\mathcal{D}_{x_{x_e}}^\mu \left[{}^{(2)}\mathcal{P}_{k+1}^\mu(x) \right] \right)_{\Omega_\varepsilon}, \\ \mathbf{M}_{kp}^{(\varepsilon)} &= \left(\Psi_p(x), {}^{(2)}\mathcal{P}_{k+1}^\mu(x) \right)_{\Omega_\varepsilon}, \\ \mathbf{f}_k^{(\varepsilon)} &= \left(f, {}^{(2)}\mathcal{P}_{k+1}^\mu(x) \right)_{\Omega_\varepsilon}, \end{aligned} \quad (25)$$

are respectively the *history*, local stiffness, local mass matrices, and local force vector.

3.1. **Elemental (Local) Operations:** the construction of local matrices $\mathbf{S}^{(\varepsilon)}$ and $\mathbf{M}^{(\varepsilon)}$, and vector $\mathbf{f}^{(\varepsilon)}$

Here, we provide the analytically obtained expressions of the local stiffness matrix as well as the proper quadrature rules to construct the local mass matrix and force vector in the PG method.

Elemental (Local) Stiffness Matrix $\mathbf{S}^{(\varepsilon)}$: given the structure of the basis functions, we first obtain the first ($p = 0$) and last column ($p = P$) of the the local stiffness matrix $\mathbf{S}^{(\varepsilon)}$, and then, the rest of entries corresponding to the interior modes. Hence,

$$\begin{aligned} \mathbf{S}_{k0}^{(\varepsilon)} &= \int_{x_{\varepsilon-1}}^{x_\varepsilon} \frac{d\Psi_0}{dx} {}^{RL}\mathcal{D}_{x_{x_e}}^\mu \left[{}^{(2)}\mathcal{P}_{k+1}^\mu(x) \right] dx, \\ &= \text{Jac}(\varepsilon, \mu) \int_{-1}^1 \left(\frac{-1}{2} \right) \left(\frac{d\zeta}{dx} \right) \frac{\Gamma[1+k+\mu]}{\Gamma[1+k]} P_k(\zeta) \left(\frac{dx}{d\zeta} \right) d\zeta, \\ &= -\text{Jac}(\varepsilon, \mu) \frac{\Gamma(1+k+\mu)}{2\Gamma(1+k)} \int_{-1}^1 P_k(\zeta) d\zeta, \\ &= -\text{Jac}(\varepsilon, \mu) \frac{\Gamma(1+k+\mu)}{\Gamma(1+k)} \delta_{k,0}, \quad (\text{by the orthogonality}) \end{aligned} \quad (26)$$

in which the Jacobian constant, associated with the element ε and the fractional order μ , is $Jac(\varepsilon, \mu) = (\frac{2}{x_\varepsilon - x_{\varepsilon-1}})^\mu$; hence the first column of the local stiffness matrix for $\varepsilon = 1, 2, \dots, N_{el}$ is obtained as

$$\mathbf{S}_{k0}^{(\varepsilon)} = -\left(\frac{2}{x_\varepsilon - x_{\varepsilon-1}}\right)^\mu \frac{\Gamma(1+k+\mu)}{\Gamma(1+k)} \delta_{k,0}, \quad k = 0, 1, \dots, P. \quad (27)$$

Similarly, we can obtain the last column of the local stiffness matrix $\mathbf{S}_{kP}^{(\varepsilon)}$ as

$$\mathbf{S}_{kP}^{(\varepsilon)} = \left(\frac{2}{x_\varepsilon - x_{\varepsilon-1}}\right)^\mu \frac{\Gamma(1+k+\mu)}{\Gamma(1+k)} \delta_{k,0} = -\mathbf{S}_{k0}^{(\varepsilon)}, \quad k = 0, 1, \dots, P. \quad (28)$$

In order to obtain the rest of entries of $\mathbf{S}_{kp}^{(\varepsilon)}$ ($k = 0, 1, \dots, P$ and $p = 1, 2, \dots, P-1$), we carry out the integration-by-parts and transfer another derivative onto the test function, taking into account that the interior modes vanish at the boundary points x_ε and $x_{\varepsilon-1}$. Therefore,

$$\begin{aligned} \mathbf{S}_{kp}^{(\varepsilon)} &= \int_{x_{\varepsilon-1}}^{x_\varepsilon} \frac{d\Psi_p}{dx} {}^{RL}\mathcal{D}_{x_\varepsilon}^\mu \left[({}^{(2)}\mathcal{P}_{k+1}^\mu(x)) \right] dx, \\ &= - \int_{x_{\varepsilon-1}}^{x_\varepsilon} \Psi_p(x) \frac{d}{dx} {}^{RL}\mathcal{D}_{x_\varepsilon}^\mu \left[({}^{(2)}\mathcal{P}_{k+1}^\mu(x)) \right] dx, \\ &= - \int_{-1}^1 \Psi_p(\zeta) \frac{d}{d\zeta} \frac{d\zeta}{dx} Jac(\varepsilon, \mu) {}^{RL}\mathcal{D}_1^\mu \left[({}^{(2)}\mathcal{P}_{k+1}^\mu(\zeta)) \right] \frac{dx}{d\zeta} d\zeta, \\ &= -Jac(\varepsilon, \mu) \frac{\Gamma(1+k+\mu)}{4\Gamma(1+k)} \int_{-1}^1 (1-\zeta)(1+\zeta) P_{p-1}^{1,1}(\zeta) \frac{d}{d\zeta} \left[P_k(\zeta) \right] d\zeta, \\ &= -Jac(\varepsilon, \mu) \frac{\Gamma(1+k+\mu)}{4\Gamma(1+k)} \frac{k+1}{2} \int_{-1}^1 (1-\zeta)(1+\zeta) P_{p-1}^{1,1}(\zeta) P_{k-1}^{1,1}(\zeta) d\zeta. \end{aligned} \quad (29)$$

Hence, for $\varepsilon = 1, 2, \dots, N_{el}$,

$$\mathbf{S}_{kp}^{(\varepsilon)} = -\left(\frac{2}{x_\varepsilon - x_{\varepsilon-1}}\right)^\mu \frac{\Gamma(1+k+\mu)(k+1)}{8\Gamma(1+k)} C_{k-1}^{1,1} \delta_{k,p}, \quad \begin{array}{l} k = 0, \dots, P, \\ p = 1, \dots, P-1, \end{array} \quad (30)$$

where $C_{k-1}^{1,1}$ represents the corresponding orthogonality constant of Jacobi polynomials of order $k-1$ with parameters $\alpha = \beta = 1$. We note that the entries of $\mathbf{S}_{kp}^{(\varepsilon)}$

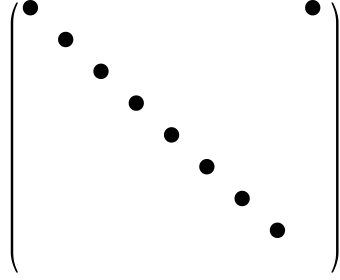


Figure 3: Sparsity of local stiffness matrix

are obtained analytically using the orthogonality of Jacobi polynomial. Also, the interior modes lead to a *diagonal* matrix due to $\delta_{k,p}$. Fig. 3 shows the sparsity of the local stiffness matrix.

Elemental (Local) Mass Matrix $\mathbf{M}^{(\varepsilon)}$: similarly, we first obtain the corresponding first ($p = 0$) and last column ($p = P$) of the local mass matrix $\mathbf{M}^{(\varepsilon)}$, and then, we compute the rest of entries associated with the interior modes.

$$\begin{aligned} \mathbf{M}_{k0}^{(\varepsilon)} &= \int_{x_{\varepsilon-1}}^{x_{\varepsilon}} \Psi_0(x) {}^{(2)}\mathcal{P}_{k+1}^{\mu}(x) dx, \\ &= \left(\frac{x_{\varepsilon} - x_{\varepsilon-1}}{2}\right) \int_{-1}^1 \Psi_0(\zeta) {}^{(2)}\mathcal{P}_{k+1}^{\mu}(\zeta) d\zeta, \\ &= \frac{1}{2} \left(\frac{x_{\varepsilon} - x_{\varepsilon-1}}{2}\right) \int_{-1}^1 (1 - \zeta)^{1+\mu} P_k^{\mu, -\mu}(\zeta) d\zeta. \end{aligned}$$

Hence, for $\varepsilon = 1, 2, \dots, N_{el}$,

$$\mathbf{M}_{k0}^{(\varepsilon)} = \left(\frac{x_{\varepsilon} - x_{\varepsilon-1}}{4}\right) \sum_{q=1}^Q w_q^{1+\mu, 0} P_k^{\mu, -\mu}(z_q^{1+\mu, 0}), \quad k = 0, 1, \dots, P,$$

where $\{w_q^{1+\mu, 0}, z_q^{1+\mu, 0}\}_{q=1}^Q$ are the Gauss-Lobatto-Jacobi weights and points corresponding to the parameters $\alpha = 1 + \mu$ and $\beta = 0$. By similar steps, we obtain

$$\begin{aligned} \mathbf{M}_{kP}^{(\varepsilon)} &= \int_{x_{\varepsilon-1}}^{x_{\varepsilon}} \Psi_P(x) {}^{(2)}\mathcal{P}_{k+1}^{\mu}(x) dx, \\ &= \left(\frac{x_{\varepsilon} - x_{\varepsilon-1}}{2}\right) \int_{-1}^1 \Psi_P(\zeta) {}^{(2)}\mathcal{P}_{k+1}^{\mu}(\zeta) d\zeta, \\ &= \frac{1}{2} \left(\frac{x_{\varepsilon} - x_{\varepsilon-1}}{2}\right) \int_{-1}^1 (1 + \zeta)(1 - \zeta)^{\mu} P_k^{\mu, -\mu}(\zeta) d\zeta. \end{aligned}$$

Therefore, for $\varepsilon = 1, 2, \dots, N_{el}$,

$$\mathbf{M}_{kP}^{(\varepsilon)} = \left(\frac{x_\varepsilon - x_{\varepsilon-1}}{4} \right) \sum_{q=1}^Q w_q^{\mu,1} P_k^{\mu,-\mu}(z_q^{\mu,1}), \quad k = 0, 1, \dots, P,$$

where $\{w_q^{\mu,1}, z_q^{\mu,1}\}_{q=1}^Q$ are the Gauss-Lobatto-Jacobi weights and points corresponding to the parameters $\alpha = \mu$ and $\beta = 1$. The rest of the entries of the local mass matrix are then obtained as

$$\begin{aligned} \mathbf{M}_{kp}^{(\varepsilon)} &= \int_{x_{\varepsilon-1}}^{x_\varepsilon} \Psi_p(x) {}^{(2)}\mathcal{P}_{k+1}^\mu(x) dx, \\ &= \left(\frac{x_\varepsilon - x_{\varepsilon-1}}{2} \right) \int_{-1}^1 \Psi_p(\zeta) {}^{(2)}\mathcal{P}_{k+1}^\mu(\zeta) d\zeta, \\ &= \frac{1}{4} \left(\frac{x_\varepsilon - x_{\varepsilon-1}}{2} \right) \int_{-1}^1 (1 + \zeta)(1 - \zeta)^{1+\mu} P_k^{\mu,-\mu}(\zeta) d\zeta, \end{aligned}$$

and thus, for $\varepsilon = 1, 2, \dots, N_{el}$,

$$\mathbf{M}_{kP}^{(\varepsilon)} = \left(\frac{x_\varepsilon - x_{\varepsilon-1}}{8} \right) \sum_{q=1}^Q w_q^{1+\mu,1} P_k^{\mu,-\mu}(z_q^{1+\mu,1}), \quad k = 0, 1, \dots, P,$$

where $\{w_q^{1+\mu,1}, z_q^{1+\mu,1}\}_{q=1}^Q$ are the Gauss-Lobatto-Jacobi weights and points corresponding to the parameters $\alpha = 1 + \mu$ and $\beta = 1$.

Elemental (Local) Load Vector $\mathbf{f}^{(\varepsilon)}$: the local load vector is obtained as:

$$\mathbf{f}_k^{(\varepsilon)} = \int_{x_{\varepsilon-1}}^{x_\varepsilon} f(x) {}^{(2)}\mathcal{P}_{k+1}^\mu(x) dx = \left(\frac{x_\varepsilon - x_{\varepsilon-1}}{2} \right) \int_{-1}^1 (1 - \zeta)^\mu f(x(\zeta)) P_k^{\mu,-\mu}(\zeta) d\zeta.$$

Hence, for $\varepsilon = 1, 2, \dots, N_{el}$,

$$\mathbf{f}_k^{(\varepsilon)} = \left(\frac{x_\varepsilon - x_{\varepsilon-1}}{2} \right) \sum_{q=1}^Q w_q^{\mu,0} f(x_\varepsilon(\zeta_q)) P_k^{\mu,-\mu}(z_q^{\mu,0}), \quad k = 0, 1, \dots, P,$$

where $\{w_q^{\mu,0}, z_q^{\mu,0}\}_{q=1}^Q$ are the Gauss-Lobatto-Jacobi weights and points corresponding to the parameters $\alpha = \mu$ and $\beta = 0$.

3.2. *Non-Local Operation: the construction of history matrix $\hat{\mathbf{S}}^{(e,\varepsilon)}$*

The most challenging part of constructing the linear system is to compute the global history matrix $\hat{\mathbf{S}}^{(e,\varepsilon)}$. The history matrix relates the current element $\varepsilon = 1, 2, \dots, N_{el}$ to its past elements $e = 1, 2, \dots, \varepsilon - 1$ by

$$\hat{\mathbf{S}}_{kp}^{(e,\varepsilon)} = \int_{x_{e-1}}^{x_e} \frac{d\Psi_p}{dx} H_k^{(\varepsilon)}(x) dx, \quad k = 0, \dots, P, \quad p = 1, \dots, P-1, \quad (31)$$

where $H_k^{(\varepsilon)}(x)$ is given in (20) as

$$\begin{aligned} H_k^{(\varepsilon)}(x) &= \frac{-1}{\Gamma(1-\mu)} \frac{d}{dx} \int_{x_{\varepsilon-1}}^{x^\varepsilon} \frac{{}^{(2)}\mathcal{P}_{k+1}^\mu(s)}{(s-x)^\mu} ds, \\ &= \frac{-\mu}{\Gamma(1-\mu)} \int_{x_{\varepsilon-1}}^{x^\varepsilon} \frac{{}^{(2)}\mathcal{P}_{k+1}^\mu(s)}{(s-x)^{1+\mu}} ds, \end{aligned}$$

in which, $x \in \Omega_e = [x_{e-1}, x_e]$ and $s \in \Omega_\varepsilon = [x_{\varepsilon-1}, x_\varepsilon]$. By performing the following affine mappings

$$\begin{aligned} s &= \frac{x_\varepsilon + x_{\varepsilon-1}}{2} + \frac{x_\varepsilon - x_{\varepsilon-1}}{2} \zeta, \\ x &= \frac{x_e + x_{e-1}}{2} + \frac{x_e - x_{e-1}}{2} \xi, \end{aligned}$$

from Ω_e and Ω_ε to the standard element $[-1, 1]$, the history function $H_k^{(\varepsilon,e)}(\xi) = H_k^{(\varepsilon)}(x)$ is obtained as

$$\begin{aligned} H_k^{(\varepsilon,e)}(\xi) & \\ &= \left(\frac{x_\varepsilon - x_{\varepsilon-1}}{2} \right)^{-\mu} \frac{-\mu}{\Gamma(1-\mu)} \int_{-1}^1 \frac{{}^{(2)}\mathcal{P}_{k+1}^\mu(\zeta) d\zeta}{\left[\frac{(x_\varepsilon + x_{\varepsilon-1}) - (x_e + x_{e-1})}{2} + \frac{x_\varepsilon - x_{\varepsilon-1}}{2} \zeta - \frac{x_e - x_{e-1}}{2} \xi \right]^{1+\mu}}. \end{aligned} \quad (32)$$

If the mesh is ‘‘uniform’’, then

$$\begin{aligned} \frac{x_\varepsilon + x_{\varepsilon-1}}{2} &= \frac{2\varepsilon - 1}{2} \Delta x, & \frac{x_e + x_{e-1}}{2} &= \frac{2e - 1}{2} \Delta x, \\ \frac{x_\varepsilon - x_{\varepsilon-1}}{2} &= \frac{x_e - x_{e-1}}{2} = \frac{\Delta x}{2}, \end{aligned} \quad (33)$$

and thus,

$$\begin{aligned}
H_k^{(\varepsilon, e)}(\xi) &= \frac{\Delta x}{2} \frac{-\mu}{\Gamma(1-\mu)} \int_{-1}^1 \frac{{}^{(2)}\mathcal{P}_{k+1}^\mu(\zeta)}{\left[\frac{(2\varepsilon-1)-(2e-1)}{2} \Delta x + \frac{\Delta x}{2} (\zeta - \xi) \right]^{1+\mu}} d\zeta, \\
&= \frac{-\mu}{\Gamma(1-\mu)} \left(\frac{2}{\Delta x} \right)^\mu \int_{-1}^1 \frac{{}^{(2)}\mathcal{P}_{k+1}^\mu(\zeta)}{\left[2(\varepsilon - e) + \zeta - \xi \right]^{1+\mu}} d\zeta, \\
&= \frac{-\mu}{\Gamma(1-\mu)} \left(\frac{2}{\Delta x} \right)^\mu \int_{-1}^1 \frac{{}^{(2)}\mathcal{P}_{k+1}^\mu(\zeta)}{\left[2\Delta\varepsilon + \zeta - \xi \right]^{1+\mu}} d\zeta, \tag{34}
\end{aligned}$$

where $\Delta\varepsilon = \varepsilon - e > 0$, denotes the element difference between the current element ε and the e -th element. Next, we expand the poly-fractonomials ${}^{(2)}\mathcal{P}_{k+1}^\mu(\zeta)$ in terms of fractonomials $(1 - \zeta)^{\mu+m}$ as

$${}^{(2)}\mathcal{P}_{k+1}^\mu(\zeta) = (1 - \zeta)^\mu P_k^{\mu, -\mu}(\zeta) = \sum_{m=0}^k C_{km} (1 - \zeta)^{\mu+m}, \tag{35}$$

in which $C_{km} = \binom{k+m}{m} \binom{k+\mu}{k-m} \left(-\frac{1}{2}\right)^m$ is a lower-triangle matrix. Therefore, (34) can be written as

$$H_k^{(\varepsilon, e)}(\xi) = \frac{-\mu}{\Gamma(1-\mu)} \left(\frac{2}{\Delta x} \right)^\mu \sum_{m=0}^k C_{km} h_m^{(\varepsilon, e)}(\xi), \tag{36}$$

where we call

$$h_m^{(\varepsilon, e)}(\xi) \equiv \int_{-1}^1 \frac{(1 - \zeta)^{\mu+m}}{\left[2\Delta\varepsilon + \zeta - \xi \right]^{1+\mu}} d\zeta, \quad m = 0, 1, \dots, k, \tag{37}$$

the (*modal*) *memory mode*. Also, $h_m^{(\varepsilon, e)}(\xi)$ can be obtained analytically as

$$h_m^{(\varepsilon, e)}(\xi) = \frac{2(\Delta\varepsilon - \xi/2)}{1 + m + \mu} \left[h_{m,I}(\xi, \Delta\varepsilon) + h_{m,II}(\xi, \Delta\varepsilon) + h_{m,III}(\xi, \Delta\varepsilon) \right], \tag{38}$$

in which

$$\begin{aligned}
h_{m,I}(\xi, \Delta\varepsilon) &= -Z_I(\xi, \Delta\varepsilon) {}_2F_1\left(1, 1 + m, 2 + m + \mu, Z_I(\xi, \Delta\varepsilon)\right), \tag{39} \\
h_{m,II}(\xi, \Delta\varepsilon) &= \left(\frac{1 - 2\Delta\varepsilon + \xi}{-2\Delta\varepsilon + \xi} \right)^{-\mu} (2^{m+\mu}) Z_{II}(\xi, \Delta\varepsilon) {}_2F_1\left(1, 1 + m, 2 + m + \mu, Z_{II}(\xi, \Delta\varepsilon)\right), \\
h_{m,III}(\xi, \Delta\varepsilon) &= -Z_{III}(\xi, \Delta\varepsilon) {}_2F_1\left(1, 1 + m, 2 + m + \mu, Z_{III}(\xi, \Delta\varepsilon)\right),
\end{aligned}$$

and the group variables are $Z_I(\xi, \Delta\varepsilon) = \frac{1}{1+2\Delta\varepsilon-\xi}$, $Z_{II}(\xi, \Delta\varepsilon) = \frac{-2}{-1-2\Delta\varepsilon+\xi}$, and $Z_{III}(\xi, \Delta\varepsilon) = \frac{1}{-2\Delta\varepsilon+\xi}$.

Moreover, The derivative of the basis function in the standard element is given by

$$\frac{d\Psi_p(\zeta)}{d\zeta} = \begin{cases} \frac{-1}{2}, & p = 0, \\ \frac{d}{d\zeta} \left[\left(\frac{1-\zeta}{2}\right) \left(\frac{1+\zeta}{2}\right) P_{p-1}^{1,1}(\zeta) \right], & p = 1, 2, \dots, P-1, \\ \frac{1}{2}, & p = P. \end{cases} \quad (40)$$

Therefore, by (35) and (40), the entries of the history matrix can be efficiently computed using a Gauss quadrature. Hence:

$$\hat{\mathbf{S}}_{kp}^{(\varepsilon, e)} \equiv \hat{\mathbf{S}}_{kp}^{(\Delta\varepsilon)} = \int_{-1}^1 \frac{d\Psi_p}{d\xi} H_k(\xi, \Delta\varepsilon) d\xi, \quad k, p = 0, 1, \dots, P. \quad (41)$$

Remark 3.1. We note that when a uniform mesh is employed, the history function $H_k^{(\varepsilon, e)}(\xi) \equiv H_k(\xi, \Delta\varepsilon)$, defined in the standard element, only depends on the “element difference”, $\Delta\varepsilon = \varepsilon - e$. This is significant since one only needs to construct $N_{el} - 1$ history function, and thus, history matrices $\hat{\mathbf{S}}^{(e, \varepsilon)}$.

3.3. Assembling the Global System with Local Test Functions

We generalize the notion of global linear system assembly by taking into account the presence of the history stiffness matrices and recalling that the corresponding local mass matrix $\mathbf{M}^{(\varepsilon)}$ or the local load-vector $\mathbf{f}^{(\varepsilon)}$ do not contribute to any history calculations. We impose the C^0 – continuity by employing the “mapping arrays”, $\text{map}[e][p]$, defined as

$$\text{map}[e][p] = P(e-1) + p, \quad p = 1, 2, \dots, P, \quad e = 1, 2, \dots, N_{el}, \quad (42)$$

as for instance in Mathematica, the first entry of a vector is labelled by 1 rather than 0 as in C++. Then, the corresponding $(P+1) \times (P+1)$ “local” linear system, which is associated with the element Ω_ε , is obtained as

$$\mathcal{M}^{(\varepsilon)} = \mathbf{S}^{(\varepsilon)} - \lambda \mathbf{M}^{(\varepsilon)}. \quad (43)$$

We assemble the corresponding global linear matrix \mathbb{M}_G and the global load-vector \mathbb{F}_G as follows:

```

do  $\varepsilon = 1, N_{el}$ 
  do  $k = 1, P + 1$ 
     $\mathbb{F}_G [ \text{map}[\varepsilon][k] ] = \mathbf{f}^{(\varepsilon)}[k]$ 
  do  $p = 1, P + 1$ 
     $\mathbb{M}_G [ \text{map}[\varepsilon][k] ] [ \text{map}[\varepsilon][p] ] = \mathbb{M}_G [ \text{map}[\varepsilon][k] ] [ \text{map}[\varepsilon][p] ] + \mathcal{M}^{(\varepsilon)}[k][p]$ 
  do  $e = 1, \varepsilon - 1$ 
     $\mathbb{M}_G [ \text{map}[\varepsilon][k] ] [ \text{map}[e][p] ] = \mathbb{M}_G [ \text{map}[e][k] ] [ \text{map}[e][p] ] + \hat{\mathbf{S}}^{(\Delta\varepsilon)}[k][p]$ 
End

```

This global operation leads to the following linear system:

$$\boxed{\mathbb{M}_G \hat{u}_G = \mathbb{F}_G}, \quad (44)$$

in which \hat{u}_G denotes the global degrees of freedom. The homogeneous Dirichlet boundary conditions are enforced by ignoring the first and the last rows also the first and the last columns of the global matrix, in addition to ignoring the first and last entries of the load matrix. We do so since we already know that $\hat{u}_0^1 = \hat{u}_P^{N_{el}} = 0$.

3.4. Scattering from the Global to Local Degrees of Freedom

Once again, due to our C^0 -continuity and the decomposition of our basis functions into boundary and interior modes, we have $\hat{u}_P^{e-1} = \hat{u}_0^e$. That leads to the following standard scattering process from the global to local degrees of freedom (see e.g., [44]):

```

do  $\varepsilon = 1, N_{el}$ 
  do  $k = 1, P + 1$ 
     $\hat{u}^\varepsilon[k] = \hat{u}_G [ \text{map}[\varepsilon][k] ]$ 
  End

```

3.5. Off-Line Computation of History Matrices and History Retrieval

As mentioned in remark 3.1 (on uniform grid generation), the history matrices solely depend on the element difference, $\Delta\varepsilon = \varepsilon - e$. Thus, for all local elements ε , where $\varepsilon = 1, 2, \dots, N_{el}$, the history matrices corresponding to the past element e with similar element difference, are the same. See Fig. 4, where similarly-colored blocks represent the same history matrix and one can see that, for example, all

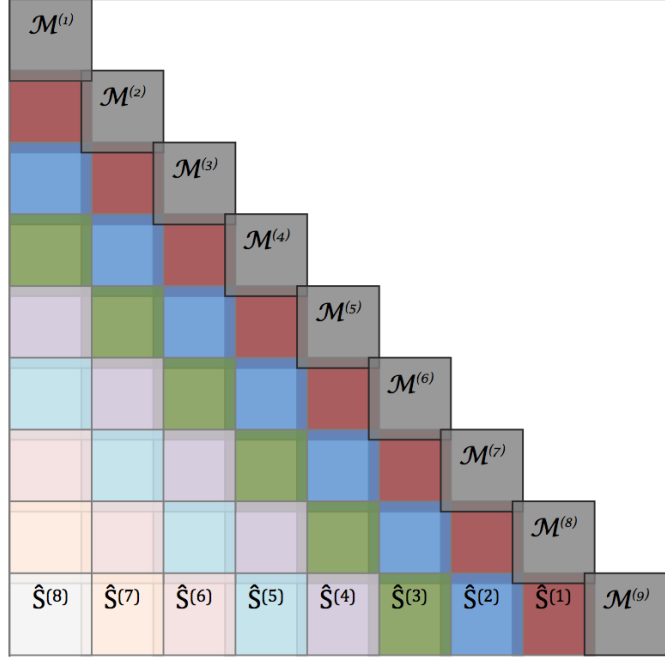


Figure 4: The assembled global matrix corresponding to a uniform grid with $N_{el} = 9$. In this global matrix, $\mathcal{M}^{(\varepsilon)} = \mathbf{S}^{(\varepsilon)} - \lambda \mathbf{M}^{(\varepsilon)}$, $\varepsilon = 1, 2, \dots, N_{el}$, represents the local matrix, associated with the element Ω_{ε} . To fill the lower-triangular block matrices, we construct only $(N_{el} - 1)$ history matrices $\hat{\mathbf{S}}^{(\Delta\varepsilon)}$, where $\Delta\varepsilon = 1, 2, \dots, N_{el} - 1$, rather than $\frac{N_{el}(N_{el}-1)}{2}$ matrices.

the history matrices adjacent to the local stiffness matrices have the same element difference, $\Delta\varepsilon = 1$, and thus are in the same color. Therefore, given number of element N_{el} , we only need to construct the total number of $N_{el} - 1$ history matrices.

For a maximum number of elements, $N_{el}|_{max}$, and a maximum number of modes, $P|_{max}$, we can compute off-line and store the total $N_{el}|_{max} - 1$ history matrices of size $(P|_{max} + 1) \times (P|_{max} + 1)$, which we can fetch later for any specific $N_{el} \leq N_{el}|_{max}$ and $P \leq P|_{max}$.

3.6. Non-Uniform Kernel-Based Grids

We present a non-uniform grid generation based on the power-law kernel in the definition of fractional derivative. There are different sources of singularity in the proposed problem that can be caused mainly due to the force function $f(x)$. However, even if the force term is smooth the underlying kernel of a fractional

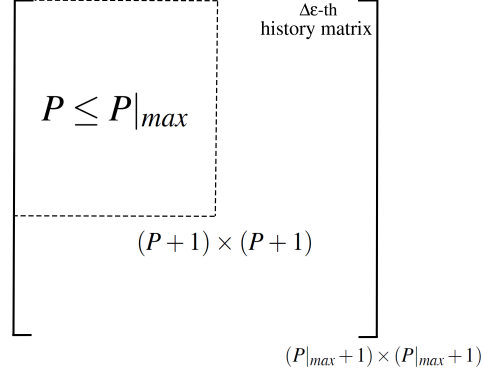


Figure 5: History computation and retrieval.

derivative leads to formation of singularities at the boundaries. Herein, we propose a new kernel-based grid generation method that considers a sufficiently small boundary layer at the vicinity of singular point and partitions that particular region non-uniformly. In this approach, we treat the kernel of the form $\frac{1}{x^\sigma}$ as a density function and then, we construct the grid such that the integral of kernel function over each element $\Omega_e \in [x_{e-1}, x_e]$ (in the boundary layer) is constant. Since

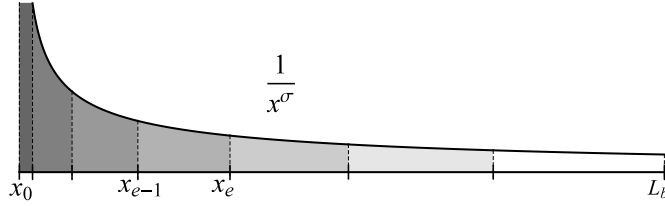


Figure 6: Kernel-based non-uniform grid in the boundary layer; L_b and N_b are the length of and the number of elements in the boundary layer, respectively.

the operator is a left sided fractional derivative, we represent the non-uniform grid refinement at the left boundary. Let L_b be the length of boundary layer and $\int_0^{L_b} \frac{1}{x^\sigma} dx = \frac{L_b^{1-\sigma}}{1-\sigma} = A$. Then, the integral over each element is

$$\frac{1}{A} \int_{x_{e-1}}^{x_e} \frac{1}{x^\sigma} dx = \frac{1}{L_b^{1-\sigma}} \left[(x_{e-1} + \Delta x_e)^{1-\sigma} - x_{e-1}^{1-\sigma} \right] = C,$$

where $\Delta x_e = x_e - x_{e-1}$ and C is a constant. Thus,

$$\Delta x_e = \left[x_{e-1}^{1-\sigma} + C L_b^{1-\sigma} \right]^{\frac{1}{1-\sigma}} - x_{e-1}.$$

Starting from $x_0 = 0$ and calculating the rest of grid locations successively, we obtain

$$x_e = \delta e^{\frac{1}{1-\sigma}}, \quad e = 1, 2, \dots, N_b, \quad \text{element numbers}, \quad (45)$$

in which $\delta = L_b C^{\frac{1}{1-\sigma}}$ and N_b is the number of elements in the boundary layer. The constant C is obtained by the constraint $\sum_{e=1}^{N_b} \Delta x_e = L_b$ and hence,

$$C = \left(\sum_{e=1}^{N_b} \left[e^{\frac{1}{1-\sigma}} - (e-1)^{\frac{1}{1-\sigma}} \right] \right)^{\sigma-1}.$$

We consider $\sigma = 1 - \mu$ and thus when $\mu = 1$, we recover the uniform grid $x_e = \frac{L_b}{N_b} e$, where the kernel is 1, $C = \frac{1}{N_b}$, $\delta = \frac{L_b}{N_b}$. Fig. 7 shows how the singularity in the kernel changes the non-uniformity in the grid.

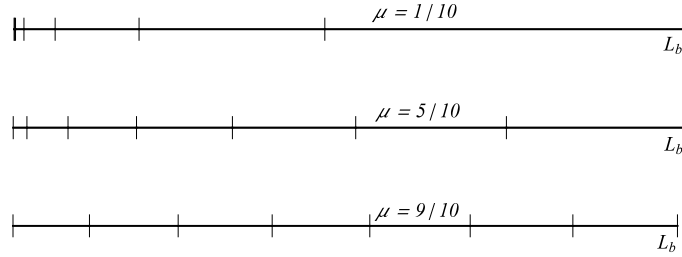


Figure 7: Non-uniform kernel-based grids for $N_b = 7$.

We note that in the boundary layer, where the grid is non-uniform, equations (33)-(39) no longer hold. Thus, using (45), we obtain

$$H_k^{(\varepsilon, e)}(\xi) = \frac{-\mu}{\Gamma(1-\mu)} \frac{\delta}{2} \left(\varepsilon^{\frac{1}{\mu}} - (\varepsilon-1)^{\frac{1}{\mu}} \right) \int_{-1}^1 \frac{{}^{(2)}\mathcal{P}_{k+1}^{\mu}(\zeta) d\zeta}{\mathcal{Z}}, \quad (46)$$

in which,

$$\begin{aligned} \mathcal{Z} = & \left(\frac{\delta}{2} \right)^{1+\mu} \left[\left(\varepsilon^{\frac{1}{\mu}} + (\varepsilon-1)^{\frac{1}{\mu}} \right) - \left(e^{\frac{1}{\mu}} + (e-1)^{\frac{1}{\mu}} \right) \right. \\ & \left. + \left(\varepsilon^{\frac{1}{\mu}} - (\varepsilon-1)^{\frac{1}{\mu}} \right) \zeta - \left(e^{\frac{1}{\mu}} - (e-1)^{\frac{1}{\mu}} \right) \xi \right]^{1+\mu}. \end{aligned}$$

Therefore, by (31) and (40), the entries of the history matrix for the boundary layer elements, where $\varepsilon = 1, 2, \dots, N_b$ and $e = 1, 2, \dots, \varepsilon - 1$, can be numerically obtained as

$$\hat{\mathbf{S}}_{kp}^{(\varepsilon, e)} = \int_{-1}^1 \frac{d\Psi_p}{d\xi} H_k^{(\varepsilon, e)}(\xi) d\xi, \quad k, p = 0, 1, \dots, P, \quad (47)$$

These matrices are the small squares in the upper left corner of Fig. 8 (interaction of boundary layer elements e and ε). For the interior elements, $\varepsilon = N_b + 1, N_b + 2, \dots, N_{el}$, when $N_b + 1 \leq e \leq \varepsilon - 1$, the grid is uniform and therefore, we use (41) to obtain the history matrices. These matrices are shown as the big squares in Fig. 8 (interaction of interior elements e and ε). However, when $1 \leq e \leq N_b$, the grid is non-uniform and we use (47) to obtain the history matrices. These matrices are shown as skinny rectangles in Fig. 8 (interaction of interior elements with boundary layer elements).

In uniform grid generation, the history function (34) only depends on element difference $\Delta\varepsilon$, which leads to a fast and efficient construction of history matrices (see Remark 3.1). However, in non-uniform kernel-based grid generation, this is not the case anymore and construction of history matrices is computationally expensive. Improving the history construction on non-uniform grids requires further investigations, to be done in our future works.

3.7. Non-Uniform Geometrically Progressive Grids

In addition to the non-uniform grid generation based on the kernel of fractional derivative, we consider a non-uniform grid using geometrically progressive series [47, 48]. In this case, the length of elements are increased by a constant factor r (see Fig. 9). By considering the length of first element to be δ , we construct the grid as $x_0 = 0$, $x_1 = \delta$, $x_2 = \delta(1 + r)$, $x_3 = \delta(1 + r + r^2)$ and so on. Hence,

$$x_e = \delta \sum_{i=0}^{e-1} r^i = \delta \frac{r^e - 1}{r - 1}, \quad e = 1, 2, \dots, N_b. \quad (48)$$

Choosing r and N_b , the constant δ is obtained by the constraint $x_{N_b} = L_b$, which gives $\delta = L_b \frac{r-1}{r^{N_b}-1}$. Since the grid is non-uniform, equations (33)-(39) do not hold anymore. Thus, using (48), we obtain

$$H_k^{(\varepsilon, e)}(\xi) = \frac{-\mu}{\Gamma(1-\mu)} \left(\frac{2}{\delta}\right)^\mu r^{\Delta\varepsilon - \mu(e-1)} \int_{-1}^1 \frac{{}^{(2)}\mathcal{P}_{k+1}^\mu(\zeta) d\zeta}{\left[\frac{r+1}{r-1}(r^{\Delta\varepsilon} - 1) + (\zeta - r^{\Delta\varepsilon}\xi)\right]^{1+\mu}}, \quad (49)$$

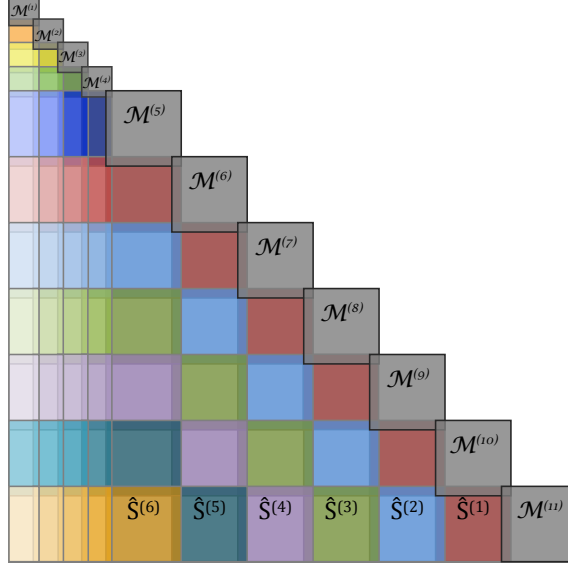


Figure 8: The assembled global matrix corresponding to $N_{el} = 11$ with $N_b = 4$ non-uniform boundary elements and 7 uniform interior elements. In this global matrix, $\mathcal{M}^{(\varepsilon)} = \mathbf{S}^{(\varepsilon)} - \lambda \mathbf{M}^{(\varepsilon)}$, $\varepsilon = 1, 2, \dots, N_{el}$, represents the local matrix, associated with the element Ω_ε . The lower-triangle consists of three parts: 1) The small square $\frac{N_b(N_b-1)}{2}$ history matrices (interaction of boundary elements, $\varepsilon = 1, 2, \dots, N_b$). 2) The big square history matrices (interaction of interior elements, $\varepsilon = N_b + 1, \dots, N_{el}$). 3) The skinny rectangular $(N_{el} - N_b)N_b$ history matrices (interaction of boundary elements with interior elements).

where $\Delta\varepsilon = \varepsilon - e > 0$, denotes the *element difference* between the current element ε and the e -th element. Using the same expansion as in (35), we can write (49) as

$$H_k^{(\varepsilon, e)}(\xi) = \frac{-\mu}{\Gamma(1-\mu)} \left(\frac{2}{\delta}\right)^\mu r^{\Delta\varepsilon - \mu(e-1)} \sum_{m=0}^k C_{km} \tilde{h}_m^{(\varepsilon, e)}(\xi), \quad (50)$$

where the (modal) memory mode

$$\tilde{h}_m^{(\varepsilon, e)}(\xi) = \int_{-1}^1 \frac{(1-\zeta)^{\mu+m}}{\left[\frac{r+1}{r-1}(r^{\Delta\varepsilon} - 1) + (\zeta - r^{\Delta\varepsilon}\xi)\right]^{1+\mu}} d\zeta, \quad m = 0, 1, \dots, k, \quad (51)$$

can be obtained analytically using hypergeometric functions. Therefore, by (50) and (40), the entries of the history matrix can be efficiently computed using the

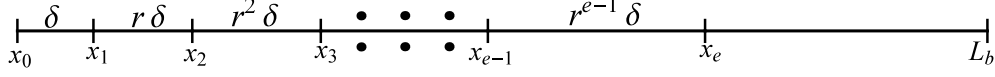


Figure 9: Non-uniform geometrically progressive grid.

Gauss quadrature in (41). The construction of the assembled global linear system is the same as kernel-based grid generation approach. We note that similar to uniform grid, in the non-uniform grid generation using the geometrical progression, the history functions depend on the element difference $\Delta\varepsilon = \varepsilon - e$, leading to a fast and efficient construction of history matrices.

4. Petrov-Galerkin Method with Global Test Functions

In this section, similar to the case of local test functions, by substituting (13) into (12) and considering the global test function, given in (17), we obtain:

$$\begin{aligned} & \sum_{e=1}^{N_{el}} \left(\sum_{p=0}^P \hat{u}_p^{(e)} \frac{d\Psi_p(x)}{dx}, {}^{RL}\mathcal{D}_L^\mu v_k^\varepsilon(x) \right)_{\Omega_e} - \lambda \sum_{e=1}^{N_{el}} \left(\sum_{p=0}^P \hat{u}_p^{(e)} \Psi_p(x), v_k^\varepsilon(x) \right)_{\Omega_e} \\ &= \sum_{e=1}^{N_{el}} \left(f, v_k^\varepsilon(x) \right)_{\Omega_e}, \quad \varepsilon = 1, 2, \dots, N_{el}, \quad k = 0, 1, \dots, P. \end{aligned} \quad (52)$$

Since the test function vanishes only $\forall x \in \Omega_e \neq \Omega_\varepsilon$ and $e > \varepsilon$, (52) reduces to

$$\begin{aligned} & \sum_{e=1}^{\varepsilon} \sum_{p=0}^P \hat{u}_p^{(e)} \left(\frac{d\Psi_p}{dx}, {}^{RL}\mathcal{D}_{x_\varepsilon}^\mu v_k^\varepsilon(x) \right)_{\Omega_e} - \lambda \sum_{e=1}^{\varepsilon} \sum_{p=0}^P \hat{u}_p^{(e)} \left(\Psi_p(x), v_k^\varepsilon(x) \right)_{\Omega_e} \\ &= \sum_{e=1}^{\varepsilon} \left(f, v_k^\varepsilon(x) \right)_{\Omega_e}. \end{aligned}$$

By substituting (17), we obtain

$$\begin{aligned} & \sum_{e=1}^{\varepsilon} \sum_{p=0}^P \hat{u}_p^{(e)} \left(\frac{d\Psi_p}{dx}, {}^{RL}\mathcal{D}_{x_\varepsilon}^\mu ({}^{(2)}\mathcal{P}_{k+1}^\mu(x^{1 \sim \varepsilon})) \right)_{\Omega_e} - \lambda \sum_{e=1}^{\varepsilon} \sum_{p=0}^P \hat{u}_p^{(e)} \left(\Psi_p(x), ({}^{(2)}\mathcal{P}_{k+1}^\mu(x^{1 \sim \varepsilon})) \right)_{\Omega_e} \\ &= \int_0^{x_\varepsilon} f(x) ({}^{(2)}\mathcal{P}_{k+1}^\mu(x^{1 \sim \varepsilon})) dx, \quad \varepsilon = 1, 2, \dots, N_{el}, \quad k = 0, 1, \dots, P, \end{aligned}$$

which can be written in the matrix form as

$$\sum_{e=1}^{\varepsilon} \sum_{p=0}^P \hat{u}_p^{(e)} \left[\hat{\mathbf{S}}_{kp}^{(\varepsilon,e)} - \lambda \hat{\mathbf{M}}_{kp}^{(\varepsilon,e)} \right] = \mathbf{f}_k^{(\varepsilon)}, \quad \varepsilon = 1, 2, \dots, N_{el}, \quad k = 0, 1, \dots, P, \quad (53)$$

where

$$\hat{\mathbf{S}}_{kp}^{(\varepsilon,e)} = \left(\frac{d\psi_p^\varepsilon}{dx}, {}^{RL}\mathcal{D}_{x_\varepsilon}^\mu \left[{}^{(2)}\mathcal{P}_{k+1}^\mu(x^{1\sim\varepsilon}) \right] \right)_{\Omega_\varepsilon}, \quad (54)$$

$$\hat{\mathbf{M}}_{kp}^{(\varepsilon,e)} = \left(\psi_p^\varepsilon(x), {}^{(2)}\mathcal{P}_{k+1}^\mu(x^{1\sim\varepsilon}) \right)_{\Omega_\varepsilon}, \quad (55)$$

$$\mathbf{f}_k^{(\varepsilon)} = \int_0^{x_\varepsilon} f(x) {}^{(2)}\mathcal{P}_{k+1}^\mu(x^{1\sim\varepsilon}) dx. \quad (56)$$

Remark 4.1. The benefit of choosing such global test functions is now clear since we can analytically evaluate ${}^{RL}\mathcal{D}_{x_\varepsilon}^\mu {}^{(2)}\mathcal{P}_{k+1}^\mu(x^{1\sim\varepsilon})$. However, we note that this choice of test functions introduces “extra” work associated with the construction of the “history mass matrix” $\hat{\mathbf{M}}^{(\varepsilon,e)}$, $\forall e = 1, 2, \dots, \varepsilon - 1$, when $\lambda \neq 0$.

Remark 4.2. The choice of global test functions leads to extra cost of quadrature carried out over the increasing-in-length domains of integration in (56). Depending on the behaviour of the force-term $f(x)$, this approach might require adaptive/multi-element quadrature rules to obtain the corresponding entries of the desired precision.

4.1. *Elemental (Local) Operations: the construction of $\mathbf{f}^{(\varepsilon)}$*

Here, the construction of the load-vector is the only operation that could be regarded as “local operations”. Hence,

$$\begin{aligned} \mathbf{f}_k^{(\varepsilon)} &= \int_0^{x_\varepsilon} f(x) {}^{(2)}\mathcal{P}_{k+1}^\mu(x^{1\sim\varepsilon}) dx \\ &= \left(\frac{x_\varepsilon}{2} \right) \int_{-1}^1 (1-\zeta)^\mu f(x^{1\sim\varepsilon}(\zeta)) P_k^{\mu,-\mu}(\zeta) d\zeta, \end{aligned}$$

and thus,

$$\mathbf{f}_k^{(\varepsilon)} = \left(\frac{x_\varepsilon}{2} \right) \sum_{q=1}^Q w_q^{\mu,0} f(x^{1\sim\varepsilon}(\zeta_q)) P_k^{\mu,-\mu}(\zeta_q^{\mu,0}),$$

where $\{w_q^{\mu,0}, \zeta_q^{\mu,0}\}_{q=1}^Q$ are the Gauss-Lobatto-Jacobi weights and points corresponding to the parameters $\alpha = \mu$ and $\beta = 0$.

4.2. **Global Operations:** the construction of $\hat{\mathbf{S}}^{(\varepsilon,e)}$ and $\hat{\mathbf{M}}^{(\varepsilon,e)}$

The corresponding stiffness and mass matrices are global in nature. We obtain their entries using proper Gauss quadrature rules.

4.3. **Assembling the Global System with Global Test Functions**

We extend the notion of global linear system assembly by taking into account the presence of the history stiffness and mass matrices. We similarly impose the C^0 – continuity by employing the same “mapping arrays”, $map[e][p]$, defined in (42). Let us define the $(P+1) \times (P+1)$ matrix

$$\hat{\mathcal{M}}^{(\varepsilon,e)} = \hat{\mathbf{S}}^{(\varepsilon,e)} - \lambda \hat{\mathbf{M}}^{(\varepsilon,e)}, \quad (57)$$

$\forall \varepsilon, e$ fixed. Then, we assemble the corresponding global linear matrix \mathbb{M}_G and the global load-vector \mathbb{F}_G as follows:

```

do  $\varepsilon = 1, N_{el}$ 
  do  $k = 1, P+1$ 
     $\mathbb{F}_G [ map[\varepsilon][k] ] = \mathbf{f}^{(\varepsilon)}[k]$ 
    do  $p = 1, P+1$ 
      do  $e = 1, \varepsilon$ 
         $\mathbb{M}_G [ map[\varepsilon][k] ] [ map[e][p] ] = \mathbb{M}_G [ map[\varepsilon][k] ] [ map[e][p] ] + \hat{\mathcal{M}}^{(\varepsilon,e)}[k][p]$ 
      end
    end
  end
End

```

This leads to a linear system similar to that in (44), shown in Fig. 10, where the homogeneous Dirichlet boundary conditions are enforced in a similar fashion as before. We note that the scattering operation follows the same steps as explained in section 3.4.

5. Numerical Examples

We consider numerical examples of the two PG schemes we have proposed. We provide examples of smooth and singular solutions with singularities at boundary points and in the interior domain, where we show the efficiency of developed schemes in capturing the singularities. We also perform the off-line computation of history matrices and show the improvement of computational cost. Moreover, we construct non-uniform kernel-based and geometrically progressive grids and present the success of the two approaches in capturing singular solutions. Furthermore, we investigate the non-local effects for different cases of history fading. In this section, we consider the computational domain $L = 1$.

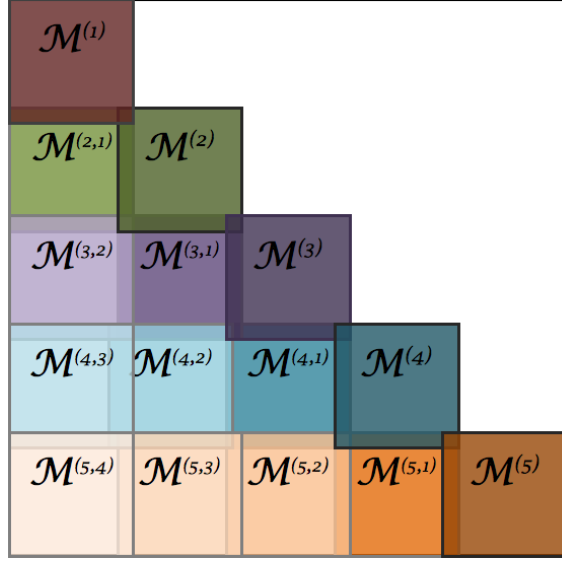


Figure 10: The assembled global matrix corresponding to $N_{el} = 5$ elements when global test functions are employed. In this global matrix, $\mathcal{M}^{(\varepsilon)} = \hat{\mathbf{S}}^{(\varepsilon)} - \lambda \hat{\mathbf{M}}^{(\varepsilon)}$, $\varepsilon = 1, 2, \dots, N_{el}$, represents the local matrix, associated with the element Ω_{ε} . To fill the lower-triangular block matrices, we must construct $\frac{N_{el}(N_{el}-1)}{2}$ history matrices $\hat{\mathbf{S}}^{(\varepsilon, e)}$.

5.1. Smooth Problems

In the proposed schemes, the choice of bases functions are polynomials, enabling the scheme to accurately and efficiently approximate the smooth solutions over the whole domain. We consider two smooth solutions of the form $u^{ext} = x^7 - x^6$ and $u^{ext} = x^6 \sin(2\pi x)$. The corresponding force functions are obtained by substituting the exact solutions into (7) (with $\lambda = 0$). By employing PG SEM, using local basis/test functions and local basis with global test functions (developed in Sec. 3 and Sec. 4, respectively), we observe that the former leads to a better approximability and condition number. Fig. 11 presents the L_2 -norm error of the PG SEM, employing local bases/test functions, where we show the exponential convergence of the scheme in approximating the two smooth solutions. The condition number of the resulting assembled global matrix, using the two developed schemes are also presented in Table 1. We show that the choice of local bases/test functions leads to a better conditioning for different number of elements and modes.

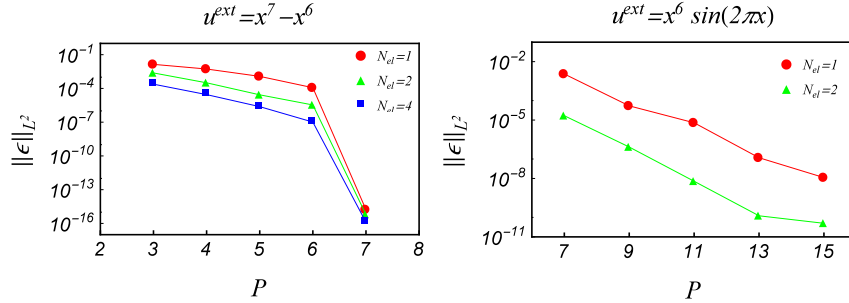


Figure 11: PG SEM with local basis/test functions. Plotted is the error with respect to the polynomial degree of each element (spectral order).

Table 1: Condition number of the resulting assembled global matrix for the two choices of local bases/test functions (left) and local bases with global test functions (right) for different number of elements and modes.

(Local Test Functions)			(Global Test Function)		
P	$N_{el} = 2$	$N_{el} = 10$	P	$N_{el} = 2$	$N_{el} = 10$
3	7.13	86.13	3	3.46×10^4	1.84×10^{16}
5	13.21	153.86	5	4.3×10^7	7.2×10^{16}
10	35.39	420.24	10	2.73×10^{15}	5.1×10^{17}

5.2. History Retrieval

As discussed in Sec. 3.5, a large number of history matrices can be computed off-line, stored, and retrieved for later use. The retrieval process, compared to on-line construction of the history matrices, leads to higher computational efficiency. In this section, by considering 1000 elements, we compute and store 999 history matrices for different number of modes, $P = 2, 3$, and 4 (here $\mu = \frac{1}{2}$). Then, for different number of elements, we compute the CPU time required for constructing and solving the linear system, obtained by retrieving the stored history matrices from hard drive. We also compute the CPU time required for constructing and solving the linear system, obtained by on-line computation of the history matrices. Table 2 shows that in the case of $p = 4$ and for $N_{el} = 10$, $N_{el} = 100$, $N_{el} = 500$, and $N_{el} = 1000$, the retrieval process is almost 4, 5, and 10 times faster, respectively. Thus, the higher p is, the faster and more efficient the retrieval becomes.

Table 2: CPU time of constructing and solving the linear system based on off-line retrieval and on-line calculation of history matrices.

CPU Time								
	$N_{el} = 10$		$N_{el} = 100$		$N_{el} = 500$		$N_{el} = 1000$	
P	Off-line retrieval	On-line computation						
2	2.6520	7.2540	24.7105	83.5229	141.3525	429.3147	370.6895	790.3478
3	4.7580	18.9073	46.0826	161.8042	266.0441	1308.8327	746.4959	4423.7671
4	8.8140	32.2922	84.8645	499.9988	485.7715	5599.4062	1392.8705	14709.4902

5.3. Singular Problems

The developed PG spectral element method, compared to single-domain spectral methods, further leads to accurate solutions even in the presence of singularities via hp -refinements at the vicinity of singularities, while still employing smooth polynomial bases. The error in the boundary layer is controlled by considering sufficient number of modes in the boundary layer elements. The error in the interior domain is then improved by performing p -refinement in those elements. In order to investigate the performance of the scheme in capturing a singularity, we consider three types of singularities, including: i) single-boundary singularity, ii) full-boundary singularity, and iii) interior singularity (when discontinuous force functions are applied).

I) Single-Boundary Singularity: we consider two singular solutions of the form $u^{ext} = (1-x)x^{2+\mu}$ and $u^{ext} = (1-x)x^{5+\mu}$ with left boundary singularity. We partition the domain into two non-overlapping elements, including one boundary element of length L_b at the vicinity of singular point in addition to an interior element for the rest of computational domain. The schematic of corresponding global system is shown in Fig. 12 (left). Table 3 shows the exponential convergence of L_2 -norm error in the interior domain. The error in the boundary layer element is then controlled by choosing sufficient number of modes in the boundary element. The results are obtained for the two cases of $L_b = 10^{-2}L$ and $L_b = 10^{-4}L$.

II) Full-Boundary Singularity: we consider the solution of the form $u^{ext} = (1-x)^{3+\mu_1}x^{3+\mu_2}$ with singular points at two ends, i.e. $x = 0$ and $x = 1$. Herein, we partition the domain into three non-overlapping elements including two boundary elements of length L_b in the vicinity of singular points, and one interior element for the rest of domain. The schematic of corresponding global system is shown in Fig. 12 (right). Similar to previous example, the PG SEM can accurately capture

the singularities at both ends, where increasing the number of modes in the interior element results in exponential convergence. Table 4 shows the L_2 -norm error in the boundary layers and interior elements with two choices of $P_b = 6, 10$ and $L_b = 10^{-2}L, 10^{-4}L$.

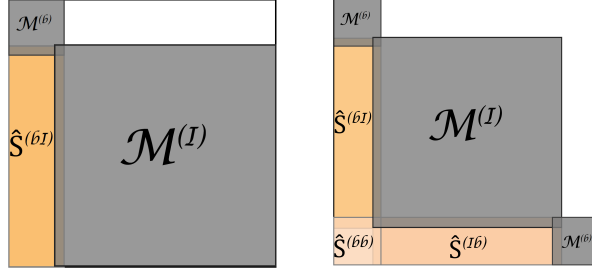


Figure 12: Schematic of global matrices corresponding to the case of singular solutions. (left): left boundary singularity, (right): left and right boundary singularities. $\hat{S}^{(bI)}$, $\hat{S}^{(Ib)}$, and $\hat{S}^{(bb)}$ denote the interaction of boundary/interior, interior/boundary and boundary/boundary elements, respectively.

III) Interior Singularity (Discontinuous Force Function): we consider the solutions with singularity in the middle of domain. The force function, obtained by substituting the solution into (7), is considered to be discontinuous at the point of singularity. Fig. 13 shows the two exact solutions of the form $u_1^{ext} = x^2(1-x)^2|x - \frac{1}{2}|$ (top) and $u_2^{ext} = \sin(3\pi x)x(1-x)|x - \frac{1}{2}|$ (bottom) and their corresponding force functions. We partition the domain at the vicinity of singular point using two non-overlapping interior elements, in which the solution is smooth. The PG scheme with local basis/test functions is shown to be able to accurately capture the singularity in the middle of the domain. In the case of u_1^{ext} , we approximate the solution in the range of machine precision with $P = 5$ within each element. We also show the exponential rate of convergence in the case of u_2^{ext} by increasing the number of modes, P , in each element. The results are shown in Fig. 14.

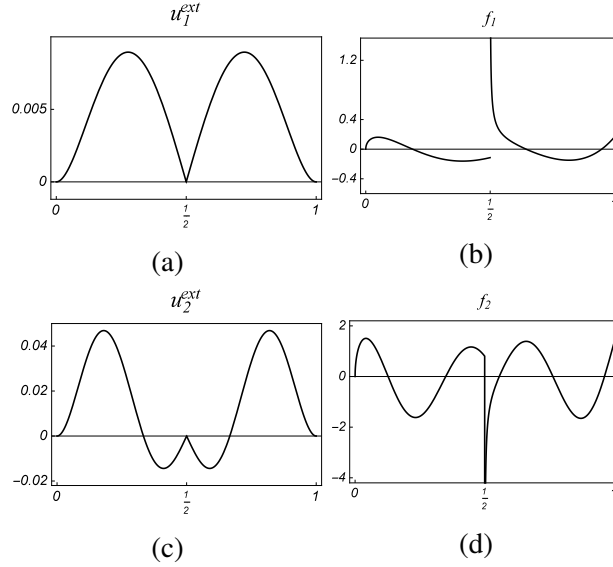


Figure 13: Interior Singularity. (left): exact solutions, (right): the corresponding force functions.

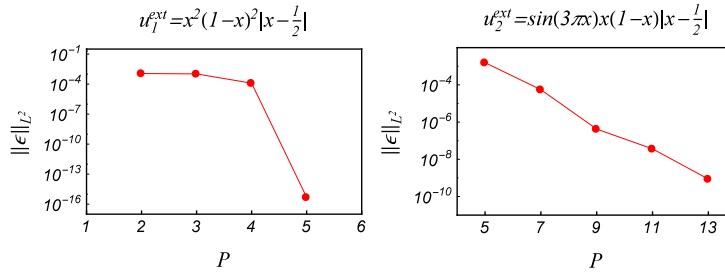


Figure 14: Interior Singularity: PG SEM with local basis/test functions. Plotted is the error with respect to spectral order in each element.

5.4. Non-Uniform Grids

We consider a singular solution of the form $u^{ext} = (1-x)x^{1+\mu}$ (here $\mu = \frac{1}{10}$ and $\lambda = 0$) with singularity at the left boundary. In order to solve the problem, we consider three grid generation approaches with similar degrees of freedom, including one uniform and two non-uniform grids over the computational domain. The non-uniform grids are generated based on the power-law kernel in the definition of fractional derivative and the geometric progression series (discussed in

Sec.3.6 and Sec.3.7, respectively). Here, we choose $L_b = L$. Table 5 shows the L_2 -norm error considering the uniform and non-uniform grids. We keep the total degrees of freedom fixed, but we increase the polynomial order P in each simulation. The success of the non-uniform grid in providing more accurate results is observed, where fewer number of elements are used, while higher order polynomial are employed. We recall that the size of boundary layer has been set to its maximum possible length, i.e. $L_b = L$. Clearly, one can obtain even more accurate results when L_b is set to much smaller length (e.g. $10^{-1}L$, $10^{-3}L$, etc.).

5.5. A Systematic Memory Fading Analysis

In order to investigate the effect of truncating the history matrices, we perform a systematic memory fading analysis.

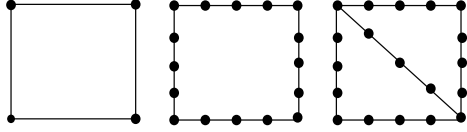
In *full* memory fading, we fade the memory by truncating the history matrices, i.e., we consider the full history matrices up to some specific number and then truncate the rest of history. For instance, we consider up to the first 4 history matrices for each element and thus compute $\hat{\mathbf{S}}^1$, $\hat{\mathbf{S}}^2$, $\hat{\mathbf{S}}^3$ and $\hat{\mathbf{S}}^4$, and truncate the rest $N_{el} - 1 - 4$ matrices; see Fig. 4 for better visualization.

In *partial* memory fading, we fade the memory by partially computing the history matrices. Similar to the *full* memory fading, we consider the full history matrices up to some specific number, however, for the rest of history matrices we partially compute the entries of matrices. In partial memory fading, we consider three different cases as follows.

- **Case I:** Boundary-Boundary (B-B) interaction. In this case, we only consider the interactions of boundary mode and boundary test functions, i.e., $p = 0, P$ and $k = 0, P$, and thus, only compute the corner entries (See Fig. 15a).
- **Case II:** Boundary-Boundary (B-B) and Boundary-Interior (B-I) interaction. In addition to the corner entries, here we also consider the interaction of boundary mode/test functions with the interior test/mode functions, i.e.,

$$\begin{cases} k = 0, & p = 0, 1, \dots, P, & \text{and} & k = P, & p = 0, 1, \dots, P \\ p = 0, & k = 0, 1, \dots, P, & \text{and} & p = P, & k = 0, 1, \dots, P, \end{cases}$$

and thus, we compute the boundary entries (See Fig. 15b).



(a) : Case I (b) : Case II (c) : Case III

Figure 15: Memory fading: (a) B-B interaction, the corner entries (b) B-B and B-I interaction, the boundary entries (c) B-B, B-I and S-I interaction, boundary and diagonal entries

- **Case III:** Boundary-Boundary (B-B), Boundary-Interior (B-I), Self-Interior (S-I) interaction. In addition to the last two cases, we consider the interaction of each mode with its corresponding test function and thus, we compute the boundaries as well as the diagonal entries (See Fig. 15c).

Tables 6 and 7 show the L_2 -norm error for cases of full and partial memory fading. It is clear from the computed norms that even in the case of fading memory, we can still accurately obtain the approximation solution, however with a proportional loss of accuracy depending on the lack of modal interaction.

6. Summary

We developed a new C^0 -continuous Petrov-Galerkin spectral element method for the problem ${}_0\mathcal{D}_x^\alpha u(x) - \lambda u(x) = f(x)$, $\alpha \in (1,2)$, subject to homogeneous boundary conditions. We obtained a weak form, in which the entire fractional derivative load was transferred onto the test functions, allowing us to efficiently employ the standard modal spectral element bases while incorporating Jacobi poly-fractonomials as the test functions. We seamlessly extended the standard procedure of assembling to *non-local assembling* in order to construct the global linear system from local (elemental) mass/stiffness matrices and non-local history matrices. The key to the efficiency of the developed PG method is twofold: i) our formulation allows the construction of elemental mass and stiffness matrices in the standard domain $[-1, 1]$ once, and ii) we efficiently obtain the non-local (history) stiffness matrices, in which the non-locality is presented *analytically*. We also investigated local basis/test functions in addition to local basis with global test functions. We demonstrated that the former choice leads to a better-conditioned system and approximability in the spectral element formulation when higher polynomial orders are needed. Moreover, we showed the exponential rate

of convergence considering smooth solutions as well as singular solutions with interior singularity; also, the spectral (algebraic) rate of convergence in singular solutions with singularities at boundaries. We also presented the retrieval process of history matrices on uniform grids, which results in faster and more efficient construction and solution of the linear system compared to the on-line computation. In addition, we constructed two non-uniform grids over the computational domain (namely, kernel-driven and geometrically progressive grids), and demonstrated the effectiveness of the non-uniform grids in accurately capturing singular solutions, using fewer number of elements and higher order polynomials. We finally performed a systematic numerical study of non-local effects via both full and partial (history) fading in order to better enhance the computational efficiency of the scheme.

Acknowledgements

The first and the second authors would like to thank Michigan State University for the generous support. The third author was supported by the MURI/ARO on Fractional PDEs for Conservation Laws and Beyond: Theory, Numerics and Applications (W911NF-15-1-0562).

References

- [1] M. Zayernouri, G. E. Karniadakis, Fractional Sturm-Liouville eigenproblems: theory and numerical approximations, *J. Comp. Physics* 47-3 (2013) 2108–2131.
- [2] R. Jha, P. K. Kaw, D. R. Kulkarni, J. C. Parikh, A. Team, Evidence of Lévy stable process in tokamak edge turbulence, *Physics of Plasmas* (1994-present) 10 (3) (2003) 699–704.
- [3] D. del Castillo-Negrete, B. A. Carreras, V. E. Lynch, Fractional diffusion in plasma turbulence, *Physics of Plasmas* (1994-present) 11 (8) (2004) 3854–3864.
- [4] A. Jaishankar, G. H. McKinley, Power-law rheology in the bulk and at the interface: quasi-properties and fractional constitutive equations, *Proceedings of the Royal Society A: Mathematical, Physical and Engineering Science* 469 (2149) (2013) 20120284.

- [5] B. Baeumer, D. A. Benson, M. Meerschaert, S. W. Wheatcraft, Subordinated advection-dispersion equation for contaminant transport, *Water Resources Research* 37 (6) (2001) 1543–1550, ISSN 1944-7973.
- [6] F. C. Meral, T. J. Royston, R. Magin, Fractional calculus in viscoelasticity: an experimental study, *Communications in Nonlinear Science and Numerical Simulation* 15 (4) (2010) 939–945.
- [7] A. Jaishankar, G. H. McKinley, A fractional K-BKZ constitutive formulation for describing the nonlinear rheology of multiscale complex fluids, *Journal of Rheology (1978-present)* 58 (6) (2014) 1751–1788.
- [8] M. Naghibolhosseini, Estimation of outer-middle ear transmission using DPOAEs and fractional-order modeling of human middle ear, Ph.D. thesis, City University of New York, NY., 2015.
- [9] J. L. Suzuki, M. Zayernouri, M. L. Bittencourt, G. E. Karniadakis, Fractional-order uniaxial visco-elasto-plastic models for structural analysis, *Computer Methods in Applied Mechanics and Engineering* 308 (2016) 443–467.
- [10] C. Lubich, On the stability of linear multistep methods for Volterra convolution equations, *IMA Journal of Numerical Analysis* 3 (4) (1983) 439–465.
- [11] C. Lubich, Discretized fractional calculus, *SIAM Journal on Mathematical Analysis* 17 (3) (1986) 704–719.
- [12] J. Sanz-Serna, A numerical method for a partial integro-differential equation, *SIAM journal on numerical analysis* 25 (2) (1988) 319–327.
- [13] N. Sugimoto, Burgers equation with a fractional derivative; hereditary effects on nonlinear acoustic waves, *J. Fluid Mech* 225 (631-653) (1991) 4.
- [14] R. Metzler, J. Klafter, The random walk’s guide to anomalous diffusion: a fractional dynamics approach, *Physics reports* 339 (1) (2000) 1–77.
- [15] R. Gorenflo, F. Mainardi, D. Moretti, P. Paradisi, Time fractional diffusion: a discrete random walk approach, *Nonlinear Dynamics* 29 (1-4) (2002) 129–143.
- [16] K. Diethelm, N. J. Ford, A. D. Freed, Detailed error analysis for a fractional Adams method, *Numerical algorithms* 36 (1) (2004) 31–52.

- [17] T. Langlands, B. Henry, The accuracy and stability of an implicit solution method for the fractional diffusion equation, *Journal of Computational Physics* 205 (2) (2005) 719–736.
- [18] Z. Sun, X. Wu, A fully discrete difference scheme for a diffusion-wave system, *Applied Numerical Mathematics* 56 (2) (2006) 193–209.
- [19] Y. Lin, C. Xu, Finite difference/spectral approximations for the time-fractional diffusion equation, *Journal of Computational Physics* 225 (2) (2007) 1533–1552.
- [20] H. Wang, K. Wang, T. Sircar, A direct $O(N \log^2 N)$ finite difference method for fractional diffusion equations, *Journal of Computational Physics* 229 (21) (2010) 8095–8104.
- [21] K. Wang, H. Wang, A fast characteristic finite difference method for fractional advection–diffusion equations, *Advances in Water Resources* 34 (7) (2011) 810–816.
- [22] J. Huang, Y. Tang, L. Vazquez, Convergence analysis of a block-by-block method for fractional differential equations, *Numer. Math. Theor. Methods Appl.* 5 (2) (2012) 229–241.
- [23] J. Cao, C. Xu, A high order schema for the numerical solution of the fractional ordinary differential equations, *Journal of Computational Physics* 238 (1) (2013) 154–168.
- [24] F. Zeng, C. Li, F. Liu, I. Turner, Numerical algorithms for time-fractional subdiffusion equation with second-order accuracy, *SIAM Journal on Scientific Computing* 37 (1) (2015) A55–A78.
- [25] M. Zayernouri, A. Matzavinos, Fractional Adams–Bashforth/Moulton methods: An application to the fractional Keller–Segel chemotaxis system, *Journal of Computational Physics* 317 (2016) 1–14.
- [26] G. Fix, J. Roof, Least squares finite-element solution of a fractional order two-point boundary value problem, *Computers & Mathematics with Applications* 48 (7) (2004) 1017–1033.
- [27] J. P. Roop, Computational aspects of FEM approximation of fractional advection dispersion equations on bounded domains in R^2 , *Journal of Computational and Applied Mathematics* 193 (1) (2006) 243–268.

- [28] V. J. Ervin, J. P. Roop, Variational formulation for the stationary fractional advection dispersion equation, *Numer. Methods Partial Differential Equations* 22 (3) (2006) 558–576.
- [29] B. Jin, R. Lazarov, J. Pasciak, Z. Zhou, Error analysis of a finite element method for the space-fractional parabolic equation, *SIAM Journal on Numerical Analysis* 52 (5) (2014) 2272–2294.
- [30] B. Jin, R. Lazarov, J. Pasciak, W. Rundell, Variational formulation of problems involving fractional order differential operators, *Mathematics of Computation* 84 (296) (2015) 2665–2700.
- [31] H. Wang, D. Yang, Wellposedness of variable-coefficient conservative fractional elliptic differential equations, *SIAM Journal on Numerical Analysis* 51 (2) (2013) 1088–1107.
- [32] H. Wang, D. Yang, S. Zhu, Inhomogeneous Dirichlet boundary-value problems of space-fractional diffusion equations and their finite element approximations, *SIAM Journal on Numerical Analysis* 52 (3) (2014) 1292–1310.
- [33] E. Hanert, A comparison of three Eulerian numerical methods for fractional-order transport models, *Environmental Fluid Mechanics* 10 (1-2) (2010) 7–20.
- [34] A. R. Carella, Spectral Finite Element Methods for solving Fractional Differential Equations with applications in Anomalous Transport, Ph.D. thesis, Norwegian University of Science and Technology, 2012.
- [35] W. Deng, J. S. Hesthaven, Local discontinuous Galerkin methods for fractional diffusion equations, *ESAIM: Mathematical Modelling and Numerical Analysis* 47 (6) (2013) 1845–1864.
- [36] Q. Xu, J. Hesthaven, Discontinuous Galerkin method for fractional convection-diffusion equations, *SIAM Journal on Numerical Analysis* 52 (1) (2014) 405–423.
- [37] M. Zayernouri, M. Ainsworth, G. E. Karniadakis, Tempered Fractional Sturm–Liouville EigenProblems, *SIAM Journal on Scientific Computing* 37 (4) (2015) A1777–A1800.

- [38] M. Zayernouri, G. E. Karniadakis, Discontinuous Spectral Element Methods for Time- and Space-Fractional Advection Equations, *SIAM Journal on Scientific Computing* 36 (4) (2014) B684–B707.
- [39] M. Zayernouri, M. Ainsworth, G. E. Karniadakis, A unified Petrov–Galerkin spectral method for fractional PDEs, *Computer Methods in Applied Mechanics and Engineering* 283 (2015) 1545–1569.
- [40] M. Zayernouri, G. E. Karniadakis, Fractional spectral collocation methods for linear and nonlinear variable order FPDEs, *Journal of Computational Physics* 293 (2015) 312–338.
- [41] M. Zayernouri, G. E. Karniadakis, Exponentially accurate spectral and spectral element methods for fractional ODEs, *J. Comp. Physics* 257 (2014) 460–480.
- [42] M. Dehghan, M. Abbaszadeh, A. Mohebbi, Legendre spectral element method for solving time fractional modified anomalous sub-diffusion equation, *Applied Mathematical Modelling* 40 (5) (2016) 3635–3654.
- [43] Y. Su, A Parallel Spectral Element Method for Fractional Lorenz System, *Discrete Dynamics in Nature and Society* 2015.
- [44] G. E. Karniadakis, S. J. Sherwin, *Spectral/hp element methods for CFD*, Oxford University Press (2nd edition), 2005.
- [45] K. S. Miller, B. Ross, *An Introduction to the Fractional Calculus and Fractional Differential Equations*, New York, NY:John Wiley and Sons, Inc., 1993.
- [46] I. Podlubny, *Fractional Differential Equations*, San Diego, CA, USA: Academic Press, 1999.
- [47] I. Babuška, M. Suri, The p and h-p versions of the finite element method, basic principles and properties, *SIAM review* 36 (4) (1994) 578–632.
- [48] M. Ainsworth, J. T. Oden, *A posteriori error estimation in finite element analysis*, vol. 37, 2011.

Table 3: Single-Boundary Singularity: L_2 -norm error in the boundary and interior elements using PG SEM with local basis/test functions. Here, L_b represents the size of left boundary element, P_b and P_I denote the number of modes in the boundary and interior elements respectively.

$$u^{ext} = (1-x)x^{2+\mu}, \quad \mu = 1/2$$

Boundary Element Error			
P_b	$L_b = 10^{-1}L$	$L_b = 10^{-2}L$	$L_b = 10^{-4}L$
6	1.29387×10^{-7}	1.29634×10^{-10}	1.19525×10^{-16}
10	1.46601×10^{-8}	1.4193×10^{-11}	4.07955×10^{-18}

Interior Element Error, $P_b = 10$			
P_I	$L_b = 10^{-1}L$	$L_b = 10^{-2}L$	$L_b = 10^{-4}L$
6	5.49133×10^{-6}	2.6893×10^{-5}	3.38957×10^{-5}
10	9.39045×10^{-8}	1.08594×10^{-6}	1.91087×10^{-6}
14	8.27224×10^{-8}	1.13249×10^{-7}	3.02065×10^{-7}

$$u^{ext} = (1-x)x^{5+\mu}, \quad \mu = 1/2$$

Boundary Element Error			
P_b	$L_b = 10^{-1}L$	$L_b = 10^{-2}L$	$L_b = 10^{-4}L$
6	3.94221×10^{-11}	2.96862×10^{-17}	4.8243×10^{-29}
10	7.07024×10^{-13}	2.54089×10^{-18}	2.26939×10^{-29}

Interior Element Error, $P_b = 10$			
P_I	$L_b = 10^{-1}L$	$L_b = 10^{-2}L$	$L_b = 10^{-4}L$
6	1.73622×10^{-5}	3.80264×10^{-5}	4.13249×10^{-5}
10	1.3122×10^{-9}	8.76951×10^{-9}	1.10139×10^{-8}
14	4.39611×10^{-12}	1.07775×10^{-10}	1.66044×10^{-10}

Table 4: Full-Boundary Singularity: L_2 -norm error in the boundary element (BE) and interior element (IE) by PG SEM with local basis/test functions. Here, $u^{ext} = (1-x)^{3+\mu_1}x^{3+\mu_2}$ with $\mu_1 = \frac{1}{4}$, $\mu_2 = \frac{2}{3}$, L_b represents the size of left and right boundary elements, P_b and P_l denote the number of modes in the boundary and interior elements respectively.

$L_b = 10^{-2}L$				$L_b = 10^{-4}L$			
$P_b = 6$				$P_b = 6$			
P_l	Left BE Error	IE Error	Right BE Error	P_l	Left BE Error	IE Error	Right BE Error
6	2.73893×10^{-7}	6.52605×10^{-5}	3.51075×10^{-6}	6	3.61679×10^{-10}	5.85397×10^{-5}	4.60538×10^{-8}
10	2.46964×10^{-11}	1.52215×10^{-7}	2.2902×10^{-9}	10	1.2676×10^{-10}	2.43295×10^{-7}	1.62151×10^{-10}
14	3.08719×10^{-12}	9.30483×10^{-9}	2.69541×10^{-10}	14	1.53993×10^{-13}	2.09933×10^{-8}	1.97677×10^{-11}
$P_b = 10$				$P_b = 10$			
P_l	Left BE Error	IE Error	Right BE Error	P_l	Left BE Error	IE Error	Right BE Error
6	2.73892×10^{-7}	6.52605×10^{-5}	3.51075×10^{-6}	6	3.61679×10^{-10}	5.85397×10^{-5}	4.60538×10^{-8}
10	2.48058×10^{-11}	1.52215×10^{-7}	2.29003×10^{-9}	10	1.2676×10^{-12}	2.43295×10^{-7}	1.62151×10^{-10}
14	3.19684×10^{-12}	9.30511×10^{-9}	2.69506×10^{-10}	14	1.53993×10^{-13}	2.09933×10^{-8}	1.97677×10^{-11}

Table 5: L_2 -norm error, using uniform and non-uniform grids. The exact singular solution is $u^{ext} = (1-x)x^{1+\mu}$ with $\mu = 1/10$.

	Uniform Grid	Kernel-Based Non-Uniform Grid	Geometrically Progressive Non-Uniform Grid
$N_{el} = 50, P = 2$	5.83943×10^{-4}	2.33461×10^{-5}	3.93956×10^{-4}
$N_{el} = 25, P = 4$	3.04739×10^{-5}	1.77458×10^{-7}	1.38755×10^{-6}
$N_{el} = 10, P = 10$	1.39586×10^{-5}	2.10813×10^{-9}	1.45695×10^{-9}

Table 6: Full history fading: L_2 -norm error using PG SEM with local basis/test functions, where $u^{ext} = x^7 - x^6$, $N_{el} = 19$, $P = 6$. The first column in the table shows the number of fully faded history matrices.

# faded history matrices	Full fading		
	$\mu = 1/10$	$\mu = 1/2$	$\mu = 9/10$
0	9.26034×10^{-12}	2.31391×10^{-11}	4.24903×10^{-9}
2	7.8905×10^{-11}	1.26365×10^{-10}	4.25456×10^{-9}
5	1.42423×10^{-8}	6.39474×10^{-8}	1.95976×10^{-8}
8	2.69431×10^{-7}	2.47423×10^{-6}	8.45001×10^{-7}
11	2.09737×10^{-6}	3.19995×10^{-5}	1.37959×10^{-5}
14	9.07427×10^{-6}	2.44911×10^{-4}	1.40684×10^{-4}
17	2.94001×10^{-5}	1.39043×10^{-3}	1.6001×10^{-3}

Table 7: Partial history fading: L_2 -norm error using PG SEM with local basis/test functions, where $u^{ext} = x^7 - x^6$, $N_{el} = 19$, $P = 6$. The first column in the tables shows number of partially faded history matrices.

Partial fading case I			
# faded history matrices	$\mu = 1/10$	$\mu = 1/2$	$\mu = 9/10$
0	9.26034×10^{-12}	2.31391×10^{-11}	4.24903×10^{-9}
2	7.8905×10^{-11}	1.26365×10^{-10}	4.25456×10^{-9}
5	1.42423×10^{-8}	6.39474×10^{-8}	1.95976×10^{-8}
8	2.69431×10^{-7}	2.47423×10^{-6}	8.45001×10^{-7}
11	2.09737×10^{-6}	3.19995×10^{-5}	1.37959×10^{-5}
14	9.07427×10^{-6}	2.44911×10^{-4}	1.40684×10^{-4}
17	2.94001×10^{-5}	1.39043×10^{-3}	1.6001×10^{-3}

Partial fading case II			
# faded history matrices	$\mu = 1/10$	$\mu = 1/2$	$\mu = 9/10$
0	9.26034×10^{-12}	2.31391×10^{-11}	4.24903×10^{-9}
2	9.27241×10^{-12}	2.34361×10^{-11}	4.2491×10^{-9}
5	3.37716×10^{-11}	6.6476×10^{-10}	4.44832×10^{-9}
8	3.8092×10^{-10}	1.99961×10^{-8}	1.36941×10^{-8}
11	1.47228×10^{-9}	2.2715×10^{-7}	1.47786×10^{-7}
14	1.15821×10^{-8}	1.64103×10^{-6}	1.47098×10^{-6}
17	5.06103×10^{-7}	7.87929×10^{-6}	1.85274×10^{-5}

Partial fading case III			
# faded history matrices	$\mu = 1/10$	$\mu = 1/2$	$\mu = 9/10$
0	9.26034×10^{-12}	2.31391×10^{-11}	4.24903×10^{-9}
2	9.26023×10^{-12}	2.3113×10^{-11}	4.24903×10^{-9}
5	1.18462×10^{-11}	7.7854×10^{-11}	4.23683×10^{-9}
8	1.60656×10^{-10}	3.38055×10^{-9}	3.65689×10^{-9}
11	1.32413×10^{-9}	4.35421×10^{-8}	8.84638×10^{-9}
14	7.10271×10^{-9}	3.87096×10^{-7}	1.7226×10^{-7}
17	2.87023×10^{-8}	3.71057×10^{-6}	5.12104×10^{-6}